



TAMPEREEN TEKNILLINEN YLIOPISTO
TAMPERE UNIVERSITY OF TECHNOLOGY

ARTUR SOSSIN

HIP IMPLANT METAL ARTIFACT REDUCTION FOR PELVIC CT
SCANS

Master's Thesis

Examiners: Professor Hannu Eskola,
Jarkko Ojala, Lic. Sci. (Tech.)
Examiners and topic approved by the
Faculty Council of Natural Sciences
on 6th of March 2013.

ABSTRACT

TAMPERE UNIVERSITY OF TECHNOLOGY

Degree Programme in Biomedical Engineering

Sossin, Artur: Hip Implant Metal Artifact Reduction in Pelvic CT Scans

Master of Science Thesis, 63 pages

March 2013

Major subject: Medical Physics

Examiners: Professor Hannu Eskola, Jarkko Ojala, Lic. Sci. (Tech.)

Keywords: Computed Tomography (CT), radiotherapy, Computational Environment for Radiotherapy Research (CERR), Hounsfield Unit (HU), linear interpolation (LI), Channel fusion metal artifact reduction (CFMAR)

Radiotherapy utilizes Computed Tomography (CT) data to perform structure contouring and dose calculations in the treatment planning process. Considerations are drawn to patients with high atomic number (high-Z) materials present in their bodies: dental fillings, hip prostheses, surgical rods, spinal cord fixation devices, et cetera. The high-Z materials introduce beam hardening artifact to CT datasets which, in combination with scatter and edge effects, produces the so called metal artifact. As a result, the dose computation accuracy is compromised and structure delineation may become cumbersome.

In order to improve the metal artifact corrupted pelvic CT images used in radiotherapy treatment planning, a novel metal artifact reduction (MAR) method was designed. The algorithm incorporated several components to deal with various distortions caused by metal present in patient anatomy. The method was tested on two CT datasets containing a single and double metallic hip prosthesis, respectively. Visual assessment of corrected CT images was carried out. Additionally, mean and standard deviation were measured in homogeneous soft and fat tissue regions in the distorted image area.

Qualitative analysis of the processed images indicated a significant improvement in anatomical tissue Hounsfield Unit (HU) accuracy, especially in the double hip implant case. This was further confirmed through the quantitative measurements which showed mean values much closer to the theoretical tissue HU value ranges. Furthermore, an up to 95% decrease in standard deviations of homogeneous tissue regions indicated a substantially lower level of artifact induced discontinuities. Finally, visual assessment of the images corrected by the proposed MAR method reflected a partial or complete restoration of bladder, bone and muscle tissue, patient body and metal object contours.

Although the MAR approach proposed in this work provided an incomplete restoration of the metal artifact corrupted CT images, the improvements made after processing are still substantial. However, it remains a matter of future work to quantitatively assess the impact on dose calculation accuracy in radiotherapy.

PREFACE

This Master of Science thesis has been conducted at the Department of Oncology at Tampere University hospital.

Firstly, I would like to express my sincere gratitude to both my supervisors Professor Hannu Eskola and Jarkko Ojala, Lic. Sci. (Tech.), for giving me the opportunity to work on such a challenging and interesting project and for providing the necessary guidance and support whenever needed. I also give a special thanks to my friends, Mirvjen Olloni and Defne Us, for giving extensive feedback on my thesis and for the support and encouragement that they have expressed.

I owe my gratitude to my dear family, my mother Jelena Šuljakova, my grandmothers Valentina Sosin and Tamara Kalashnikova, my grandfathers Pavel Sosin and Isaak Vainstein, my brother Daniel Šuljakov. The love and support they provided in difficult times gave the strength and dedication needed to perform at my best in this project.

Finally, I would like to thank my girlfriend, Jelena Demidova, for always being loving, patient and supportive throughout the course of this work.

Tampere, May 2013

Artur Sossin

LIST OF SYMBOLS

| | |
|---------------------------------|--|
| $b(x, y)$ | back-projection |
| $B\{\cdot\}$ | back-projection operator |
| $BF\{\cdot\}$ | bilateral filtering operation |
| C_p | normalization factor for the bilateral filter |
| C_M | constant specifying the metal intensity |
| $\delta(\cdot)$ | Dirac delta function |
| d | slice plane dimension of the imaged section of patient anatomy |
| ε | point from the metal interval ε_{Metal} |
| ε_{Metal} | metal interval $[\varepsilon_{\varphi,l}, \varepsilon_{\varphi,l} + \Delta\varepsilon_{\varphi,l}]$ in a projection vector taken at an angle φ |
| $\varepsilon_{\varphi,l}$ | start point of a metal interval l |
| $\Delta\varepsilon_{\varphi,l}$ | width of a metal interval l |
| $F\{\cdot\}$ | Fourier Transform operator |
| $F^{-1}\{\cdot\}$ | inverse Fourier Transform operator |
| $GB\{\cdot\}$ | Gaussian blurring operation |
| $GBF\{\cdot\}$ | gradient modified bilateral filtering operation |
| $G_\sigma(\cdot)$ | Gaussian kernel with a standard deviation σ |
| $H(i)$ | grayscale image intensity distribution, histogram |
| $H(w)$ | frequency response of the filtered back-projection filter function |
| $HU_{i,j}$ | Hounsfield Unit of pixel (i, j) |
| I | x-ray intensity after passing through the material |
| I_0 | x-ray intensity before passing through the material |
| I_t | grayscale intensity threshold |
| $I(\mathbf{p})$ | grayscale image |
| $I_{BF}(\mathbf{p})$ | grayscale image after bilateral filtering |
| $I_{GB}(\mathbf{p})$ | grayscale image after Gaussian blurring |
| $I_{GBF}(\mathbf{p})$ | grayscale image after application of the gradient modified bilateral filter |
| $I_{LI}(\mathbf{p})$ | grayscale image reconstructed from a linearly interpolated sinogram |
| $I_{MAR}(\mathbf{p})$ | metal artifact reduced grayscale image |
| μ | attenuation coefficient |
| $\mu_{i,j}$ | attenuation coefficient of pixel (i, j) |
| $\mu_{m,n}$ | attenuation coefficient of voxel (m, n) |
| μ_{H_2O} | attenuation coefficient of water |
| $\mu(x, y)$ | attenuation coefficient distribution function for a single slice |
| $\mu(x, y, z)$ | attenuation coefficient distribution function |
| $M(\mathbf{p})$ | metal mask image |
| $M(u, v)$ | Fourier Transform of $\mu(x, y)$ |
| $M_h(\mathbf{p})$ | metal mask image obtained by applying the high threshold to $I(\mathbf{p})$ |
| $M_l(\mathbf{p})$ | metal mask image obtained by applying the low threshold to $I(\mathbf{p})$ |
| \mathbf{p} | pixel $[x, y]$ |

| | |
|--------------------------------|--|
| p_{R_r} | ray sum |
| $p(r, \varphi)$ | Radon Transform space, projection space, sinogram |
| $\hat{p}(r, \varphi)$ | filtered projection at a fixed angle φ |
| $p(r, \varphi_0)$ | projection at angle φ_0 , projection vector |
| $p(r_0, \varphi_0)$ | ray integral |
| $p_{LI}(\varepsilon, \varphi)$ | linearly interpolated projection value at point (ε, φ) |
| $P(w, \varphi)$ | Fourier Transform of a projection at a fixed angle φ |
| r | distance from the coordinate origin point |
| R_r | ray taken at distance r from the coordinate origin |
| $R\{\cdot\}$ | Radon Transform operator |
| t | material thickness |
| $T\{\cdot\}$ | thresholding operation |
| φ | projection angle |
| w | spatial frequency |
| w_N | Nyquist spatial frequency |
| ∇ | gradient operator |
| $\ \cdot\ $ | Euclidean distance |

LIST OF ACRONYMS

| | |
|--------|---|
| 1D | one-dimensional |
| 2D | two-dimensional |
| 3D | three-dimensional |
| AAPM | American Association of Physicists in Medicine |
| AP | anteroposterior |
| ART | Algebraic Reconstruction Technique |
| BF | bilateral filter |
| BP | back-projection |
| CERR | Computational Environment for Radiotherapy Research |
| CFMAR | Channel Fusion Metal Artifact Reduction |
| Co | cobalt |
| CPU | central processing unit |
| Cr | chromium |
| CT | Computed Tomography |
| DAS | data acquisition system |
| DICOM | Digital Image and Communications in Medicine |
| DSP | digital signal processing |
| EEGE | exponential edge gradient effect |
| FBP | filtered back-projection |
| FCDD | fractional-order curvature driven diffusion |
| FDK | Feldkamp-Davis-Kress |
| Fe | iron |
| FOV | field of view |
| FT | Fourier Transform |
| GBF | gradient modified bilateral filter |
| GPU | graphics processing unit |
| high-Z | high atomic number |
| HU | Hounsfield Unit |
| kVp | peak kilovoltage |
| LI | linear interpolation |
| linac | linear accelerator |
| MAR | metal artifact reduction |
| MAF | multidimensional adaptive filtering |
| MLEM | Maximum Likelihood Expectation Maximization |
| Mo | molybdenum |
| MRI | Magnetic Resonance Imaging |
| NLM | non-local means |
| PA | posteroanterior |
| PACS | Picture Archiving and Communications System |
| PDE | partial differential equation |

| | |
|-------|-----------------------------------|
| PET | Photon Emission Tomography |
| Pt | platinum |
| px | pixel |
| ROI | region of interest |
| RT | Radon Transform |
| SPECT | Single Photon Emission Tomography |
| Ti | titanium |
| TPS | treatment planning system |
| TV | total variation |

TABLE OF CONTENTS

| | | |
|--------|---|----|
| 1. | Introduction | 2 |
| 2. | Background | 3 |
| 2.1. | Computed Tomography..... | 3 |
| 2.1.1. | CT system overview..... | 4 |
| 2.1.2. | Projection acquisition..... | 5 |
| 2.1.3. | Image reconstruction..... | 9 |
| 2.1.4. | CT image display | 15 |
| 2.2. | Metal artifact in CT images..... | 16 |
| 2.2.1. | Hip implant metal artifact | 19 |
| 2.2.2. | Impact on radiotherapy treatment planning | 21 |
| 2.3. | Metal artifact reduction techniques | 23 |
| 3. | Materials and Methods | 26 |
| 3.1. | Materials..... | 26 |
| 3.2. | Channel Fusion Metal Artifact Reduction | 27 |
| 3.2.1. | Slice detection | 27 |
| 3.2.2. | Slice processing..... | 28 |
| 3.2.3. | Filtering..... | 29 |
| 3.2.4. | Metal segmentation..... | 32 |
| 3.2.5. | Sinogram interpolation..... | 33 |
| 3.2.6. | Channel weighting | 34 |
| 3.3. | CFMAR performance analysis..... | 36 |
| 4. | Results..... | 37 |
| 4.1. | Qualitative Evaluation..... | 38 |
| 4.1.1. | De-noising | 42 |
| 4.1.2. | Metal Segmentation | 43 |
| 4.1.3. | Reduction of streaking | 45 |
| 4.2. | Quantitative Evaluation..... | 47 |
| 4.2.1. | The single implant case..... | 47 |
| 4.2.2. | The double implant case | 49 |
| 5. | Discussion | 51 |
| 5.1. | De-noising performance..... | 51 |
| 5.2. | Segmentation of metallic parts..... | 52 |
| 5.3. | Reduction of streaking | 54 |
| 5.4. | Computational speed..... | 57 |
| 5.5. | Future work | 58 |
| 6. | Conclusion | 59 |
| | References | 60 |

1. INTRODUCTION

Tomographic imaging modalities stand at the core of non-invasive patient diagnosis today. Techniques such as Computed Tomography (CT), Single Photon Emission Tomography (SPECT) and Positron Emission Tomography (PET) apply ionizing radiation to acquire images of internal body structures. In comparison Magnetic Resonance Imaging (MRI) uses radio frequency magnetic waves for imaging which do not cause cellular damage unlike ionizing radiation. [1; 2; 3]

CT is one of the oldest tomographic imaging techniques having been commercially established since the early 1970s. With the growth of computing capabilities, advances in x-ray detector technologies and introduction of novel reconstruction algorithms, CT imaging has become significantly faster, safer and more informative. [2; 3; 4] Currently it has grown into a frequently used diagnostic procedure for cancer diagnosis and is at the heart of radiotherapy treatment planning [1; 2; 5]. For such applications the quality of obtained images becomes exceptionally critical. The purity of CT images can be compromised through a variety of artifacts including noise, beam hardening, motion, metal artifacts and others. [1; 3; 6]

Radiotherapy uses CT data to perform structure contouring and dose calculations. Considerations are drawn in radiotherapy treatment planning to patients with high atomic number (high-Z) materials present in their bodies: dental fillings, hip prostheses, surgical rods, spinal cord fixation devices, et cetera. The high-Z materials introduce beam hardening artifact to CT datasets which, in combination with scatter and edge effects, produces the so called metal artifact. As a result, the dose computation accuracy is reduced and structure delineation may become cumbersome. A survey of 30 institutions conducted by the American Association of Physicists in Medicine (AAPM) Radiotherapy Committee indicated about 1%-4% of patients to have a prosthetic device with potential to influence the scheduled radiotherapy treatment. [7] Therefore it is of essence to explore techniques with the ability to correct for the artifacts produced by various metallic prostheses.

The dependence of metal artifact severity and topology on patient anatomy and implant types and materials introduces difficulties in determining a generic metal artifact reduction (MAR) technique. Thus, the main objective of this thesis was constrained with developing a MAR method capable to deal with the artifacts that arise in pelvic CT scans with hip prostheses. In addition the developed algorithm was intended to work as part of Computational Environment for Radiotherapy Research (CERR) open source software platform [8].

2. BACKGROUND

In order to form the theoretical basis essential for understanding the subject studied by this work, several key concepts must be discussed. These include CT (Chapter 2.1), metal artifact in CT images (Chapter 2.2) and MAR techniques (Chapter 2.3).

Chapter 2.1 introduces the principles behind projection acquisition and tomographic image reconstruction. Then, in Chapter 2.2, the reader is presented with an overview of the CT image metal artifact and its manifestation in pelvic CT scans. Finally, a literature review on some of the existing MAR methods is given in Chapter 2.3.

2.1. Computed Tomography

X-ray CT was historically the first tomographic imaging modality entirely based on digital reconstruction of images [1; 3]. It occupies a significant niche in clinical diagnosis with the application fields ranging from cancer diagnosis to extremities and osteoporosis [1]. CT enables the formation of a detailed digital representation of the selected part of the human body. The acquired images are slices of the patient's anatomy. Thus, the two-dimensional (2D) CT images are representations of three-dimensional (3D) sections located within the body (Figure 2.1). [1]

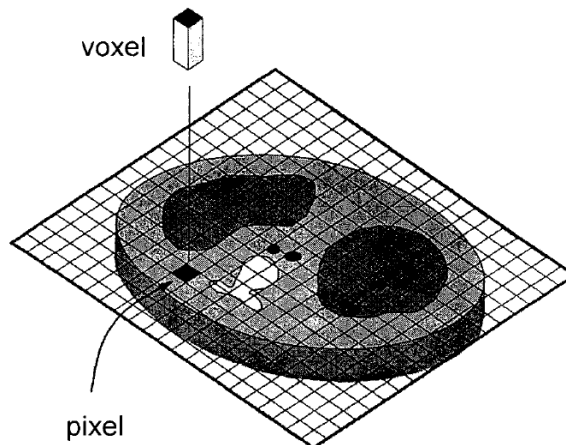


Figure 2.1. 3D representation of a single CT slice. Tomographic images are typically square arrays containing 512×512 picture elements (pixels). Each pixel represents at least 4096 possible intensity values (12 bits), however, broader intensity ranges are also possible (14 bits or 16 bits). Each pixel in the image corresponds to a voxel (volume element). The voxel has two dimensions corresponding to the ones of the pixel in the plane of the image, and the third dimension represents the slice thickness of the CT image. [1] Adapted from Bushberg et al. [1].

The pixels (px) in the image presented in Figure 2.1 convey the information about the average x-ray attenuation in the corresponding voxels in the body. Since the attenua-

tion varies among different tissues, the resultant image will provide intensity based separation for different anatomical structures such as bone, muscle tissue, fat tissue, organs and cavities. Unlike planar digital x-ray images, which acquire a 2D projection of the 3D anatomical data, CT images avoid the superimposing of different anatomical structures in an image by having a small slice thickness (3 mm on average), thus, making them far more informative. [1; 3; 9]

Chapters 2.1.1-2.1.4 examine the structure of a typical x-ray tomographic scanner as well as the physical and mathematical foundation for CT image acquisition.

2.1.1. CT system overview

Although differences between the structure and functionality of commercial x-ray CT scanners may be present, the general architecture and scanner component interactions are primarily the same. The schematic in Figure 2.2 shows an overview of the x-ray tomographic system composition [9].

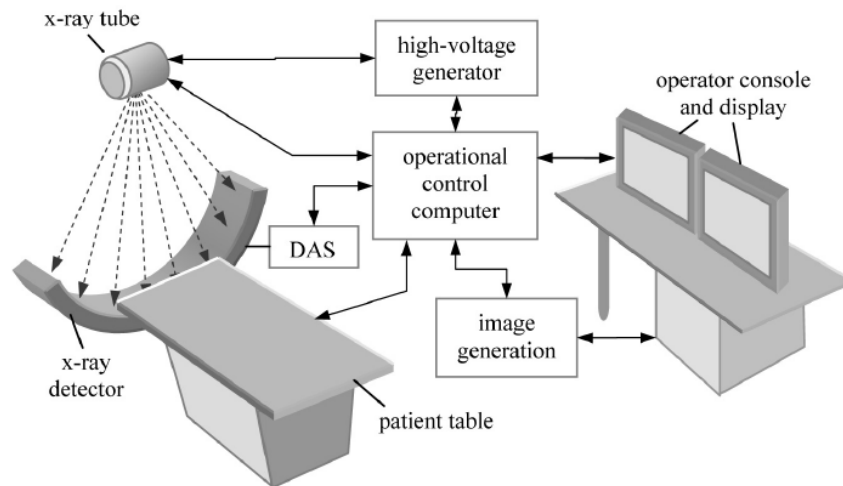


Figure 2.2. Schematic of a CT system. Modified from Hsieh et al. [9].

The acquisition of a CT image dataset is initiated with the operator positioning the patient on the CT table and conducting a *scanogram* (or *topogram*) or scout view. The main rationale behind this scan is to determine the patient's anatomical landmarks and the exact position and range of CT slices. In this scan mode both the x-ray tube and the detector remain stationary while the patient table travels at a constant speed. The scan is similar to a conventional plane x-ray taken either at an anteroposterior/posteroanterior (AP/PA) position (tube is located in front or behind the patient, respectively) or a lateral position (with the tube located on the side of the patient). Upon scout view scan initiation, an operational control computer instructs the gantry to rotate to the desired orientation as prescribed by the operator. Afterwards, instructions from the computer are transmitted to the x-ray generation and detection system, the patient table and the image generation (reconstruction) system to perform a scan. After reaching the starting scan location, the patient table maintains a constant speed during the CT dataset acquisition

sequence. The high-voltage generator shortly reaches the desired voltage (~ 120 kV) and keeps both the voltage and the current to the x-ray tube at the prescribed level during the scan. The tube generates x-ray flux, and the x-ray photons are detected by an array of solid state or gas detectors to produce electrical signals. [1; 3; 9] During this time, the data acquisition system (DAS) uniformly samples the detector outputs and transforms the incoming analog signals into digital signals. The resulting digital data is then sent to the image reconstruction system. Typically, this module consists of high-speed computers and digital signal processing (DSP) chips. Once the images are reconstructed, pre-processing and enhancement are performed. Finally, the processed data is sent to the operator workstation for viewing and to the data storage device for archiving. [9] The storage device can be the hard-drive of the workstation and/or a Picture Archiving and Communications System (PACS) server [1].

Upon the determination of the precise slice set location and range, the operator prescribes CT scans based either on preset or newly created protocols. These protocols determine x-ray tube voltage and current, gantry speed, collimator and detector apertures, scan mode, table index speed, reconstruction field of view (FOV) and kernel, and significant amount of other parameters. With the selected scanning protocol at hand, the control computer sends a series of commands to the x-ray generation and detection system, gantry and the image reconstruction module in a manner similar to that discussed for the scanogram operation. The key difference between the processes is that the x-ray CT gantry must now reach and maintain a stable rotational speed during the entire dataset acquisition. Because of its large weight (more than several hundred kilograms), it takes time for the gantry to reach stability. Therefore, the gantry is generally one of the first system components responding to the scan command. The other CT image generation sequences are similar to the ones outlined for the scanogram operation. [9]

Scanner operation may differ in various clinical applications: extremities, interventional procedures and contrast-enhanced scanning. Although mostly third generation scanners are in clinical use today, there are machines of other generations present on the market. This provides an additional source for the deviations in CT scanner operation as various generations may be characterized by different architecture. [1; 2; 3; 9]

A more detailed description of the x-ray CT system components and different scanner generations can be found in the books of Bushberg et al. [1], Jan et al. [3] and Hsieh et al. [9].

2.1.2. Projection acquisition

In order for the CT system to approximate the attenuation coefficient values of each voxel in the imaged section of the human body (Figure 2.1), x-ray projections need to be collected at various angles [1; 2; 3; 9].

Consider a spatial distribution of the attenuation coefficient values in the Cartesian coordinate system $\mu(x, y, z)$. Restricting the distribution to a slice plane ($z = z_0$), one obtains $\mu(x, y, z = z_0)$ which for simplicity of notation will be further denoted as

$\mu(x, y)$. The set of parallel x-rays located at a various distances from the origin point ($r \in (-\infty, +\infty)$) and traversing the object with the specified distribution at various projection angles ($\varphi \in (0, 2\pi)$) may be approximated by the *Radon Transform* (RT) [3]:

$$p(r, \varphi) = \int_{-\infty}^{+\infty} \int_{-\infty}^{+\infty} \mu(x, y) \delta(x \cos \varphi + y \sin \varphi - r) dx dy, \quad (2.1)$$

where $p(r, \varphi)$ denotes the RT space and $\delta(\cdot)$ is the Dirac delta function. The transform has been proven to be invertible by J. Radon in 1917. The quantity $p(r, \varphi)$ is also known by other names like *projection space* or *sinogram* [1; 2; 3; 9].

Geometrical meaning of the described integral transform plays a key role in understanding the relationship between $p(r, \varphi)$ and $\mu(x, y)$ (Figure 2.3).

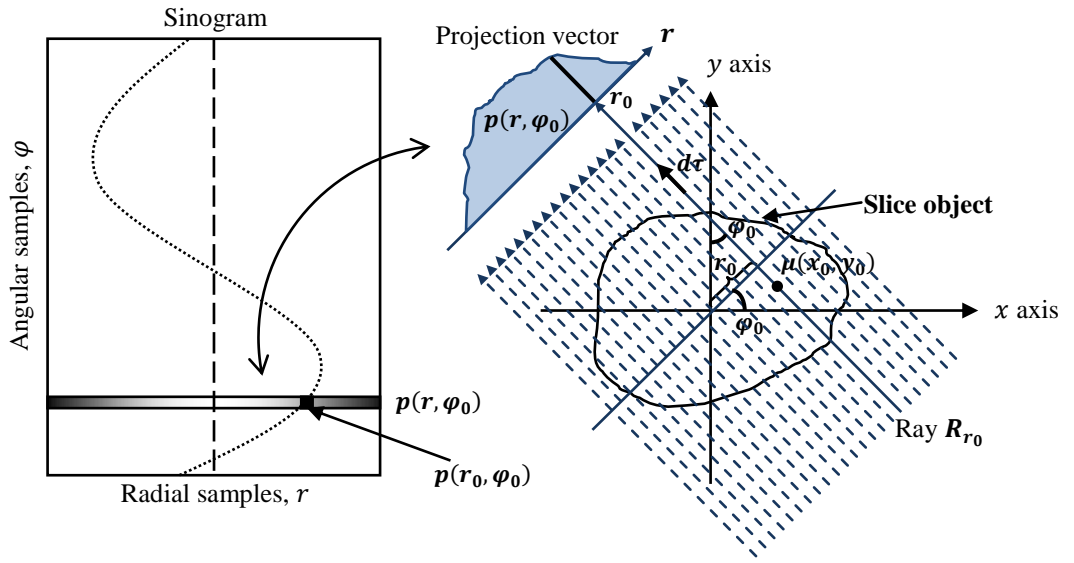


Figure 2.3. Geometrical representation of the projection vector generation and sinogram formation.

As seen from Figure 2.3, the RT space is a collection of *projection vectors* (or simply projections) acquired at various angles φ . Given an auxiliary set of coordinates r, τ rotated at a fixed angle φ_0 and a ray R_{r_0} penetrating the object at a distance r_0 from the coordinate origin, the projection vector value at r_0 can be given as [3]:

$$p(r_0, \varphi_0) = \int_{R_{r_0}} \mu(x, y) d\tau \quad (2.2)$$

This integral is called a *ray integral* which characterizes the overall attenuation along the ray R_{r_0} . Assuming an arbitrary choice of r_0 , one can express the projection vector as a function of ray integrals [3]:

$$p(r, \varphi_0) = \int_{R_r} \mu(x, y) d\tau \quad (2.3)$$

From Figure 2.3 and (2.3) it is apparent that every point (r, φ) in the projection space holds the value of a particular ray integral. Coming back to (2.1) and utilizing the schematic in Figure 2.3, one can also elaborate on the reason, why the RT space is most commonly known as the sinogram: for a fixed point (x_0, y_0) the ray passing through that point will exhibit a sinusoidal dependence of the distance r as a function of the view angle φ [1]. Hence the rays passing through the point (x_0, y_0) will produce projection vector values mapped into a sinusoidal trajectory in the sinogram. The amplitude of the sine curve will depend on the maximum displacement from the central point of the coordinate system.

As seen previously (Figure 2.3), the RT provides a mapping between the projection space $p(r, \varphi)$ and the attenuation coefficient distribution on a fixed slice $\mu(x, y)$. Thus, if one were to acquire an infinite number of projections of the slice, it would be possible to obtain $\mu(x, y)$ via the RT inverse. The operation of applying the inverse RT to the sinogram data is called *image reconstruction* [1; 2; 3; 9]. The concept of reconstruction will be considered in more detail in Chapter 2.1.3.

A schematic explaining the projection acquisition for a typical third generation scanner is depicted in Figure 2.4. The x-ray tube provides a thin (1 to 10 mm) wide fan beam (30° to 60°) able to cover the complete slice of the object. A curved detector array with its centre being in the radiation focus and its individual units having equiangular spacing with respect to the radiation focus is employed to acquire the x-rays traversing the object section. The entire slice (or several slices in the case of a multislice detector array) is scanned at once. To perform this action only rotational movements around the patient are required from the detector array and the x-ray tube. The simplicity of these movements allows scanning times less than 1 second. [3]

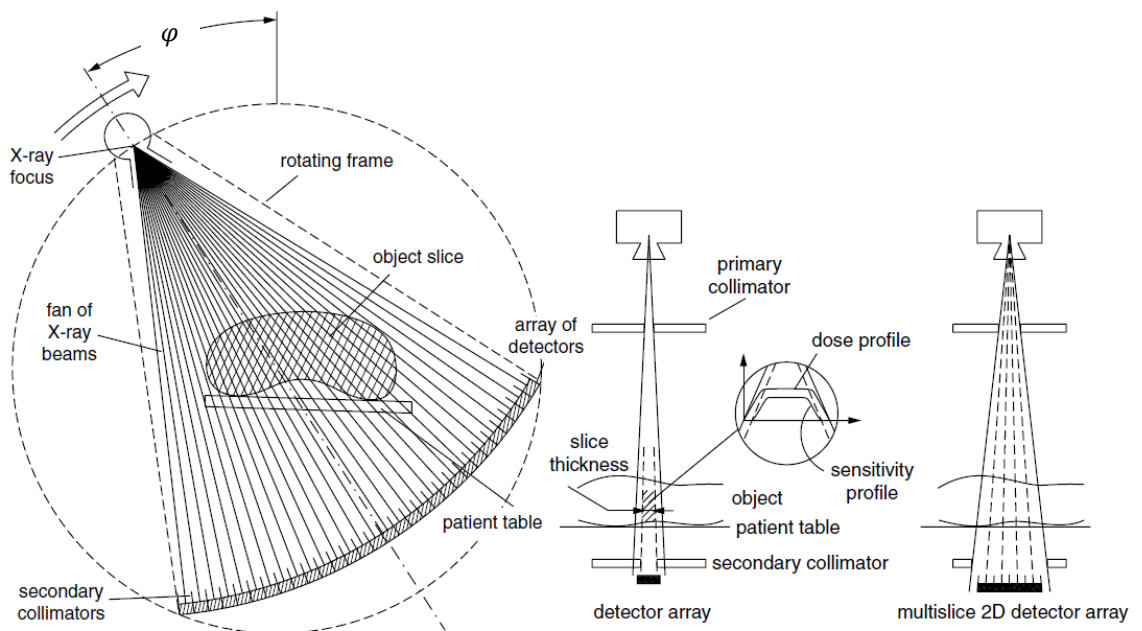


Figure 2.4. CT slice data collection process viewed in the slice plane and slice profile plane. Adapted from Jan et al. [3].

As visualized in Figure 2.4, current scanners acquire the projection data through *fan beam projection*. However, the RT concept can still be applied if the data is modified into *parallel beam projection* data. The modification is called *rebinning*. For a more detailed discussion on rebinning and fan beam geometry the reader is directed to the literature by Jan et al. [3] and Hsieh et al. [9]. From this point, parallel beam geometry will be used in any context mentioning RT throughout the thesis (Chapter 2.1.3 and Chapter 3.2).

The individual units of the detector array mentioned in Figure 2.4 measure the intensity of the incident x-rays. The intensity, I , of an x-ray passing through a material with given thickness t and attenuation coefficient value μ , is related exponentially to its initial intensity, I_0 [2]:

$$I = I_0 e^{-\mu t} \quad (2.4)$$

Assuming d and $\mu_{m,n}$ to be the slice plane dimension and attenuation coefficient of a voxel (m, n) in the imaged section of patient anatomy, respectively (Figure 2.5), one can reformulate (2.3) using (2.4) in the following manner [2]:

$$p_{R_r} = -\ln\left(\frac{I}{I_0}\right) = \sum_{R_r} \mu_{m,n} d, \quad (2.5)$$

where p_{R_r} is called a *ray sum* and is a discrete version of the ray integral mentioned in the beginning of the chapter (2.2).

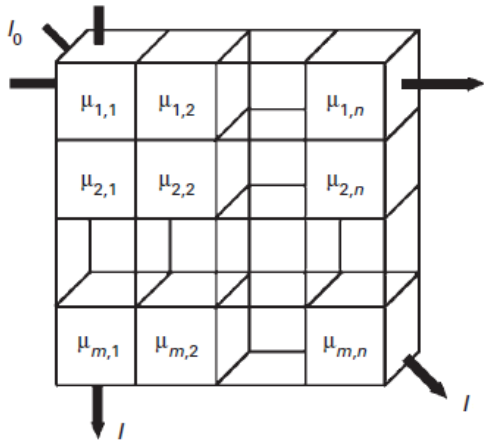


Figure 2.5. An object slice representation as a voxel matrix with a particular attenuation coefficient defined for each voxel. X-rays are depicted traversing the object slice. Adapted from Dougherty et al. [2].

From (2.5) one observes that for each detector element, if the dimension d is fixed, the initial intensity of the ray (I_0) and the intensity of the ray traversing the patient (I) are measured, then the sum of attenuation coefficients $\sum \mu_{m,n}$ along the ray incident on the detector element can be computed. Collecting the sums for rays positioned at various distances from the origin point r and at varying view angles φ enables the construc-

tion of a discrete version of the sinogram space depicted in Figure 2.3. As a result, the digital image of the patient anatomy slice can be obtained by an approximation of the discrete RT inverse [2; 3].

2.1.3. Image reconstruction

Chapter 2.1.2 introduced the concept of the RT and the objective of obtaining a slice image of the patient anatomy as an image reconstruction problem. In order to reconstruct CT images from projection data, a number of algorithm classes exist: iterative algebraic, iterative statistical and analytical [3; 4; 9].

Iterative methods aim to solve the reconstruction iteratively by starting from an initial guess of the tomographic image and then applying a correction scheme to arrive at a final solution. In iterative algebraic methods the projection data is considered as a set of linear equations where the attenuation coefficients of the individual voxels are the unknowns. Since the number of projection views and detector size are limited, one arrives at an ill-posed inverse problem where the number of unknowns is greater than the number of equations. Methods like Algebraic Reconstruction Technique (ART) aim to provide a solution to this ill-posed problem. In the case of statistical methods the aim is to model the physical processes behind x-ray acquisition through probability distributions. Such modelling arrives at the so called likelihood function in terms of the image and the sinogram which is iteratively maximized until obtaining a stable solution. Maximum Likelihood Expectation Maximization (MLEM) is a well-known example of a statistical reconstruction method. [3; 4; 9]

Analytical reconstruction methods aim to provide explicit reconstruction formulae suitable for an accurate reconstruction of images from projections. This implies fast performance. Examples include methods like *back-projection* (BP) and *filtered back-projection* (FBP). [3; 9]

Although the performance of iterative methods in terms of reconstruction accuracy is superior to that of analytical methods, the latter ones are still computationally faster and are the most used in clinical CT machines. For this reason more insight is given on BP and FBP reconstruction.

Back-projection

The BP operator forms the basis for accurate analytical reconstruction methods from projections. Given the sinogram space $p(r, \varphi)$ explained in Chapter 2.1.2, the BP is defined as follows [3]:

$$b(x, y) = \int_0^{\pi} p(r, \varphi) d\varphi, \quad (2.6)$$

where $b(x, y)$ denotes the BP image.

Both RT (2.1) and the BP (2.6) are linear operators. This implies that their impulse response is space invariant. [3] With this information at hand, one can show that the

image $b(x, y)$, obtained via the BP operation on the sinogram $p(r, \varphi)$, is equivalent to a radially smoothed version of $\mu(x, y)$ [2]:

$$b(x, y) = B\{R\{\mu(x, y)\}\} = \mu(x, y) * \left(\frac{1}{\sqrt{x^2 + y^2}} \right), \quad (2.7)$$

where $R\{\cdot\}$, $B\{\cdot\}$ and $*$ denote the RT, BP and convolution operators, respectively.

For a fixed point (r, φ) in the projection space the value of the corresponding ray integral contributes evenly to all points on the line $x \cos \varphi + y \sin \varphi = r$ in the image space. As a result, each projection vector $p(r, \varphi_0)$ is “smeared” in the direction specified by the angle φ_0 across the (x, y) plane. Thus, from (2.6) it is evident that the image obtained by the BP operation is composed of smeared projection vectors taken at different angles φ [2]. This explains the radial “blurring” described by (2.7). Image reconstruction through BP reconstruction is illustrated in Figure 2.6.

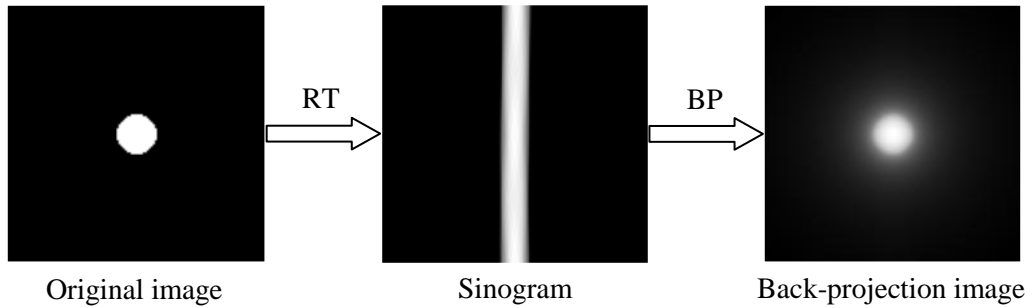


Figure 2.6. An example of BP reconstruction. Notice how the image of the circle obtained after the application of BP is radially blurred compared to the original image.

Fourier slice theorem and filtered back-projection

In order to formulate the *Fourier slice theorem* (projection slice theorem), some key definitions are required. Consider the 2D Fourier spectrum $M(u, v)$ of the previously introduced attenuation coefficient distribution function $\mu(x, y)$ [3; 9]:

$$M(u, v) = \int_{-\infty}^{+\infty} \int_{-\infty}^{+\infty} \mu(x, y) e^{-j2\pi(ux+vy)} dx dy \quad (2.8)$$

It can be shown that the one-dimensional (1D) Fourier spectrum of a projection taken at some fixed angle φ can be expressed as [3; 9]:

$$P(w, \varphi) = \int_{-\infty}^{+\infty} \int_{-\infty}^{+\infty} \mu(x, y) e^{-j2\pi w(x \cos \varphi + y \sin \varphi)} dx dy \quad (2.9)$$

The expression presented in (2.9) represents a 2D Fourier Transform (FT) of $\mu(x, y)$ with $u = w \cos \varphi$ and $v = w \sin \varphi$. With the aid of both (2.8) and (2.9) the Fourier slice theorem can now be stated: the 1D profile running through the origin point of the 2D spectrum $M(u, v)$ at the angle φ (also called the *central slice*) is equal to the 1D projection spectrum of $\mu(x, y)$ taken at the same angle [2; 3; 9].

Figure 2.7 gives an illustrative view of the Fourier slice theorem based on expressions given in (2.8) and (2.9).

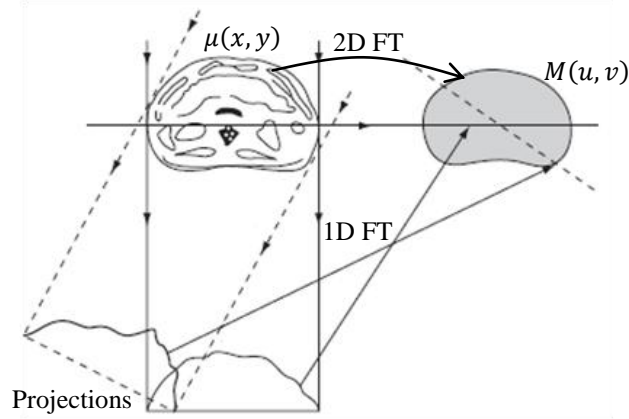


Figure 2.7. Schematic of the Fourier slice theorem. Adapted from Dougherty et al. [2].

Now that the projection slice theorem has been formulated, one can derive the FBP formula. Firstly, $\mu(x, y)$ is expressed in terms of $M(u, v)$ via the inverse FT in polar coordinates ($u = w \cos \varphi$, $v = w \sin \varphi$) [3; 9]:

$$\mu(x, y) = \int_0^{2\pi} \int_0^{\infty} M(w \cos \varphi, w \sin \varphi) e^{j2\pi w(x \cos \varphi + y \sin \varphi)} w dw d\varphi \quad (2.10)$$

Assuming that the choice of φ in (2.9) was arbitrary, the FT of the projection can be written in terms of $M(u, v)$ as follows [3; 9]:

$$P(w, \varphi) = M(w \cos \varphi, w \sin \varphi) \quad (2.11)$$

After combining (2.10) with (2.11) and applying the symmetry property of the RT, the following expression for $\mu(x, y)$ is obtained [3; 9]:

$$\mu(x, y) = \int_0^{\pi} \int_{-\infty}^{+\infty} P(w, \varphi) e^{j2\pi w(x \cos \varphi + y \sin \varphi)} |w| dw d\varphi \quad (2.12)$$

The inner integral in (2.12) is the inverse FT of a projection spectrum $P(w, \varphi)$ (which is equal to $p(r, \varphi)$) filtered linearly by a filter with a frequency response $|w|$. Thus, this integral can be called a modified or *filtered projection* $\hat{p}(r, \varphi)$. Rewriting (2.12) in terms of the filtered projection gives [3; 9]:

$$\mu(x, y) = \int_0^{\pi} \hat{p}(r, \varphi) d\varphi \quad (2.13)$$

The operation defined by (2.13) is equivalent to applying the BP operation to the filtered projections taken at various angles. Using the previously defined BP operator notation (2.7), denoting the 1D FT as $F\{\cdot\}$ and its corresponding inverse as $F^{-1}\{\cdot\}$, the

following general formula for reconstructing the attenuation coefficient distribution function $\mu(x, y)$ with FBP can be derived [3; 9]:

$$\mu(x, y) = B \left\{ F^{-1} \{ |w| F \{ p(r, \varphi) \} \} \right\} \quad (2.14)$$

From (2.14) the FBP process can be summarized as follows: filter each acquired projection $p(r, \varphi)$ and then back-project into the image space.

Filter function choice plays a key role in FBP. The frequency response of $|w|$ is characteristic to a non-restricted Ramp Filter. In practice, however, it is necessary to modify the filter function to be band-limited due to the limiting spatial resolution of the imaging system. Taking the sampling theorem into consideration, one can arrive at the conclusion that the filter bandwidth should be restricted by the upper limit equal to the Nyquist spatial frequency w_N . This gives a minimally modified Ramp Filter with the following frequency response [3]:

$$H(w) = \begin{cases} |w|, & w \in [-w_N, +w_N] \\ 0, & \text{otherwise} \end{cases} \quad (2.15)$$

From (2.15) it is straightforward to see that the carried out bandwidth restriction is equivalent to the multiplication of the theoretical frequency response $|w|$ with a rectangular unit window with a width of $2w_N$. Such action in the frequency domain corresponds to a convolution of the projection with a sinc function which can amplify the noise present within the projection. For this reason, smoother windows are more commonly applied in order to partially suppress the high frequencies below w_N , thus, providing some limitation for the noise. Such windows are, for instance, Shepp-Logan, Hamming and Cosine. [1; 2; 3; 9]

The appropriate window function depends on the application at hand. Smoothing filters provide loss of some high frequency detail and, sometimes, even residual blurring. An example application for them would be CT scans considered primarily with soft tissue imaging. The restricted ramp function can be applicable in cases dealing with bone imaging where fine detail is necessary. However, as noted earlier, this comes at the expense of a noisier image. [1; 2]

Examples of the Ramp Filters discussed previously along with some common smooth window functions used in FBP are shown below (Figure 2.8) [3].

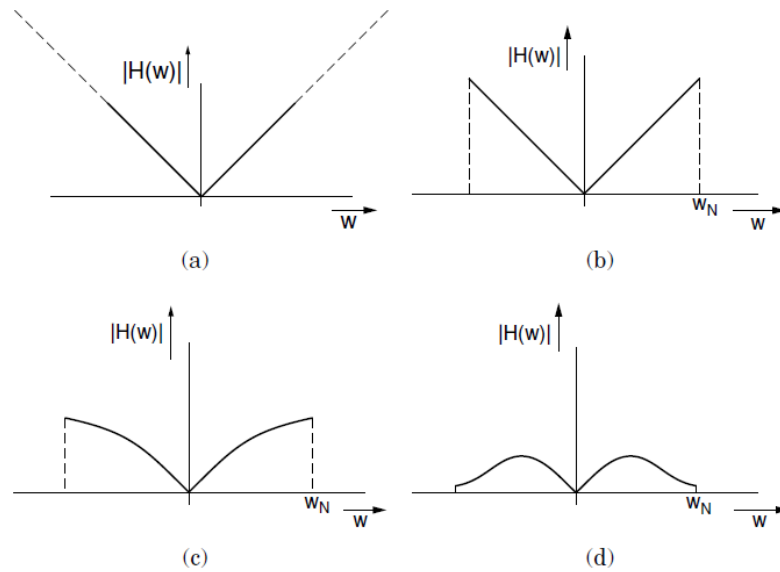


Figure 2.8. Frequency responses of various filter functions applied in FBP. The responses are displayed in terms of the spatial frequency w and the FT magnitude $|H(w)|$. The Ramp Filter (a) and its band limited version (b) are shown in the top row. The bottom row depicts two common smooth filter functions: Shepp-Logan (c) and Hamming (d). Adapted from Jan et al. [3].

From Chapter 2.1.2 it is evident that in the x-ray CT system one deals with a discrete number of projection views and radial samples. Both the BP and FBP formulae presented in this chapter have discrete counterparts that take into account the limited amount of data samples. Since the theory behind remains the same, these equations will not be presented in this thesis and the reader is referred to the works by Jan et al. [3] and Hsieh et al. [9] for information on discrete cases.

To conclude this chapter, an equivalent FBP reconstruction demonstration is presented in Figure 2.9.

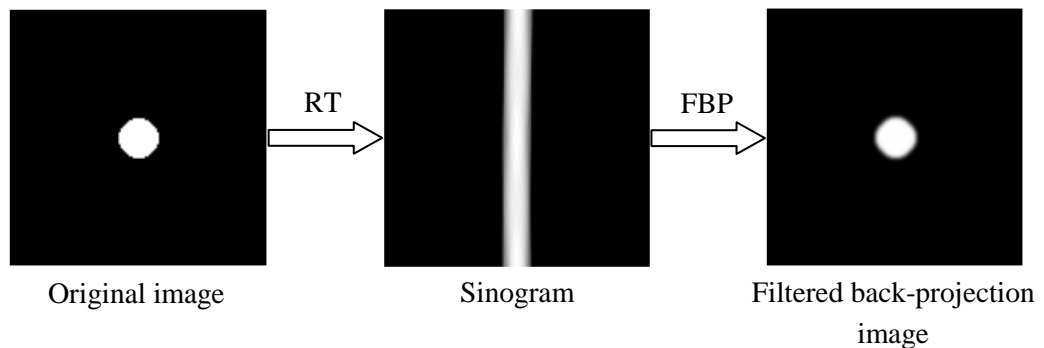


Figure 2.9. An example of FBP using the Hamming filter. Note that the reconstructed circle exhibits a low level of blurring.

From the observation of Figure 2.6 and Figure 2.9, one notes that FBP provides superior reconstruction accuracy compared to BP. The circle from Figure 2.9 exhibits a lower blurring level.

2.1.4. CT image display

The attenuation coefficients $\mu_{i,j}$ are not applied directly as the gray values of the pixels in the reconstructed image. *CT numbers* or *Hounsfield Units* (HU) are used instead. The name comes from Dr. G. N. Hounsfield, the inventor of the first x-ray CT scanner. The HU value of a pixel (i, j) is defined in terms of its attenuation coefficient $\mu_{i,j}$ and the attenuation coefficient of water μ_{H_2O} as follows [1; 2; 3; 9]:

$$HU_{i,j} = \frac{\mu_{i,j} - \mu_{H_2O}}{\mu_{H_2O}} \quad (2.16)$$

The attenuation of water is taken at x-ray energy of 72 keV by definition [3]. The HU values for different tissues are provided in the table below (Table 2.1).

Table 2.1 HU values for different tissues [2; 3; 9; 10].

| Tissue | HU value |
|--|---------------|
| Dense bone/contrast agent filled areas | +3000 |
| Cortical bone | +250 to +1000 |
| Muscle | +44 to +59 |
| Soft tissue | +10 to +50 |
| Water | 0 |
| Fat | -100 to -20 |
| Lung | -300 |
| Air | -1000 |

It must be noted, however, that among the sources used for the generation of this table, the CT number range for soft tissue and fat may vary. Additionally, for example, in the book by Hsieh et al. [9] fat is also considered as a soft tissue.

As noted previously (Figure 2.1), the pixels in tomographic images are typically given intensity values on the 12-bit grayscale (4096 intensity values), thus, enabling to map the entire range of HU values depicted in Table 2.1. This type of scale is further referred to as the *restricted HU scale*. Broader intensity ranges can also be used (14- or 16-bit), denoted further as the *unrestricted HU scale*. However, a computer monitor can only display 256 shades of gray (8-bit scale), thus, not allowing the separation between all of the HU values. This mismatch requires either that 16 CT numbers, which lie adjacent on the intensity scale, be displayed with the same gray level, in which case they become indistinguishable in the image, or that only a restricted range or *window* of HU values be visualized and used to span the 8-bit grayscale range. In this latter case, the range of CT numbers is known as the *window width* (WW) and the central value of the

range is known as the *window level* (WL). [2] It is evident that various window levels should be used to achieve adequate contrast for a given tissue [2; 9]. The idea of gray level windowing is presented below (Figure 2.10).

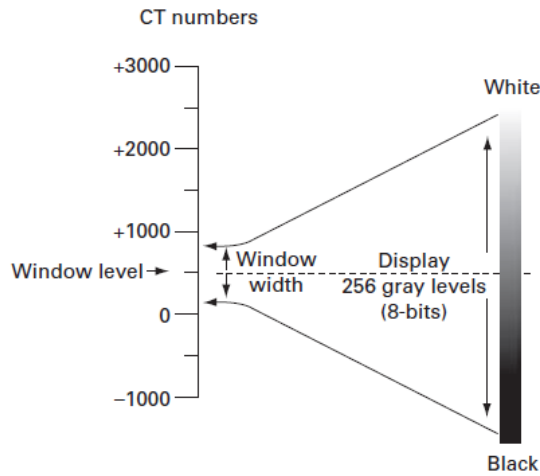


Figure 2.10. Illustration of the windowing concept. Adapted from Dougherty et al. [2].

The transformation function necessary to map the window of HU values to the 256 gray level range can be either linear or non-linear. The non-linear mapping functions provide a means to achieve contrast enhancement. A typical application of these functions is in the case of CT brain image visualization to enhance the gray and white matter differences. [9]

2.2. Metal artifact in CT images

Any discrepancy between the attenuation coefficients of the anatomical object obtained via image reconstruction from projections and the true attenuation coefficients can be defined as a *CT image artifact* [9]. X-ray CT scanners exhibit a large spectrum of artifacts (distortions) in the image due to the inherent complexity of the imaging unit design and the object being imaged (human anatomy). The following distortions are characteristic to x-ray tomographic images [1; 6; 9]: noise, scatter, aliasing, patient motion, partial volume effect, off-focal radiation, metal artifact, beam hardening, incomplete projections, wind-mill artifact, various detector related artifacts and scanner operator induced artifacts.

Since this work is concerned with the investigation of one particular CT image artifact – the *metal artifact*, a more thorough investigation of this type of image distortion will be carried out.

The causes of metal artifacts are quite complex and the appearance of this type of distortion in an image can vary significantly upon the shape and density of the metallic object. In medical applications such objects can be metallic orthopaedic hardware inside the patient – hip, leg, and arm prostheses, surgical rods, mandibular plates for reconstruction, spinal cord fixation devices, stents, and various dental fillings or equipment

attached to the patient's body – biopsy needles [7; 9]. A metal object can produce beam hardening [6; 9; 11; 12], scatter effects [6; 11; 12], noise [6; 11; 12], partial volume effect [9; 11], aliasing [9; 12], under-range in the data acquisition electronics [6; 9; 11], overflow of the dynamic range in the reconstruction process [9] and exponential edge gradient effect (EEGE) [12]. Additionally, it has been shown that motion of metal objects is a major culprit in producing distortions in CT images [6; 9; 12].

Metal artifacts are more pronounced with high-Z metals, such as platinum (Pt) or iron (Fe), and less pronounced with low atomic number metals, such as titanium (Ti). In some specific cases (such as dental fillings on head CTs), gantry tilt or patient positioning can angle the metal outside of the axial slices of interest. [6]

Out of the numerous distortions produced by metal in CT images, it is essential to study the ones most characteristic to the net metal artifact: beam hardening, scatter, EEGE and noise.

Beam hardening

Beam hardening arises from the polychromatic x-ray beam spectrum and the energy and material density dependence of attenuation coefficients. Most materials absorb low-energy x-ray photons better than they absorb high-energy ones. This is mainly due to photoelectric absorption. [9] In the case of metals the inherent high material density causes more absorption than in the case of anatomical tissue. As a result, the intensity of the rays traversing metal objects will be reduced according to (2.4). This causes the intensity values of the reconstructed CT image to be lowered in the vicinity of the metal.

Scatter

The most important interaction between x-ray photons and tissues is incoherent scattering or *Compton scattering* [5; 9]. When an x-ray photon collides with an electron, a fraction of the energy is transferred to the electron to free it from the atom and the rest of the energy is carried away by a photon. Due to momentum conservation, the scattered photon exhibits a deviation from the path of the original photon. The existence of Compton scatter implies that not all of the x-ray photons that reach the detector are primary photons. Thus, depending on x-ray CT system design, a portion of the signals in the detector will be generated by the scatter. The scattered photons make the recorded signals deviate from the true measurement of the x-ray intensities and cause either shading (streaking) artifacts or CT number shifts in the reconstructed images. [9]

Exponential edge gradient effect (EEGE)

The EEGE stems from the exponential law of x-ray attenuation (2.4), the spatial averaging resulting from the non-zero width of the scanning beam and the presence of objects with unusually high contrast and straight edges. Each CT detector measurement represents a spatial average of x-ray intensities as discussed in Chapter 2.1.2. The mathematics of reconstruction (Chapter 2.1.3) requires a similar spatial average of ray integrals of the attenuation coefficients. In most cases these averages are not equal with the inequal-

ity being most prominent in the presents of strong spatial gradients of attenuation. For this reason the effect has its name. [13]

Noise

The most common source of noise in x-ray CT is the photon flux. The x-ray photons that reach the detector determine the image noise. After passing through the patient, many of the original photons are absorbed or scattered. Since the variation in photon flux (to some approximation) corresponds to a compound *Poisson* distribution, a diminished flux measured at the detector implies a larger signal variation. Excessive photon noise can cause severe streak artifacts in most clinical situations. Poisson noise is often a consequence of inadequate patient positioning, inadequate selection of scanning parameters or simply the result of CT scanner limitations. For example, when a thin slice scan of a large patient is needed, even the highest x-ray tube voltage and current setting on the CT machine cannot deliver sufficient x-ray flux. [9]

An illustration of the basic CT image metal artifact components discussed previously is given in Figure 2.11 [11].

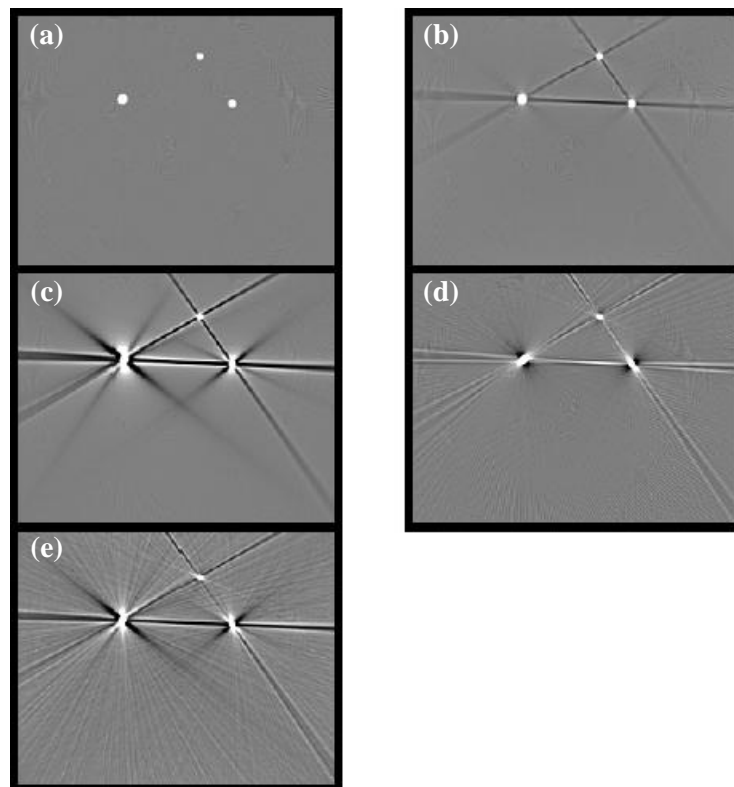


Figure 2.11. Plexiplate phantom with amalgam fillings (a) is implemented to simulate individual distortions contributing to the formation of the metal artifact. Beam hardening (b), scatter (c), EECE (d) and the overall metal artifact with noise contribution (e) are shown. Adapted from De Man et al. [11].

From Figure 2.11 it is seen that beam hardening primarily causes dark streaks in the directions of highest attenuation (Figure 2.11b). When scatter is present the dark streaks

become bordered by bright streaks (Figure 2.11c). In the case of EEGE dark and white streaks are observed connecting the edges with equally-signed and opposite gradients, respectively (Figure 2.11d). In short, the EEGE causes streaks tangent to long straight edges with a number of streaks radiating from the metals. Finally, the net effect of all three contributors with an addition of noise is visualized in Figure 2.11e resulting in significantly distorted representation of the original image shown in Figure 2.11a. [11]

2.2.1. Hip implant metal artifact

As previously noted, the metal artifact is a complex superposition of several distortions. Thus, there is a dependency of its severity not only on the shape and density of the metal, but also on the anatomy the metal is placed in. For this reason the thesis will focus on a particular case of this CT image distortion – *hip implant metal artifact*.

Hip prostheses vary in design and composition. Most total hip replacements include a prosthetic acetabular cup and a femoral component. The cup part consists of a polyethylene core supported by either a cobalt-chromium-molybdenum (Co–Cr–Mo) or Ti alloy outer shell. The femoral component is composed of head and stem parts which can be solid or hollow and made of Co–Cr–Mo, Ti alloy or steel. Some patients might have all three components, while others might have only the femoral stem implanted. [7] An image of possible hip prostheses is presented in Figure 2.12.

The majority of the current hip prosthetic devices are produced of Co–Cr–Mo alloys. Stainless steel was applied in the past, and may still be observed in patients with older implants. Ti is also implemented in some cases. [7]

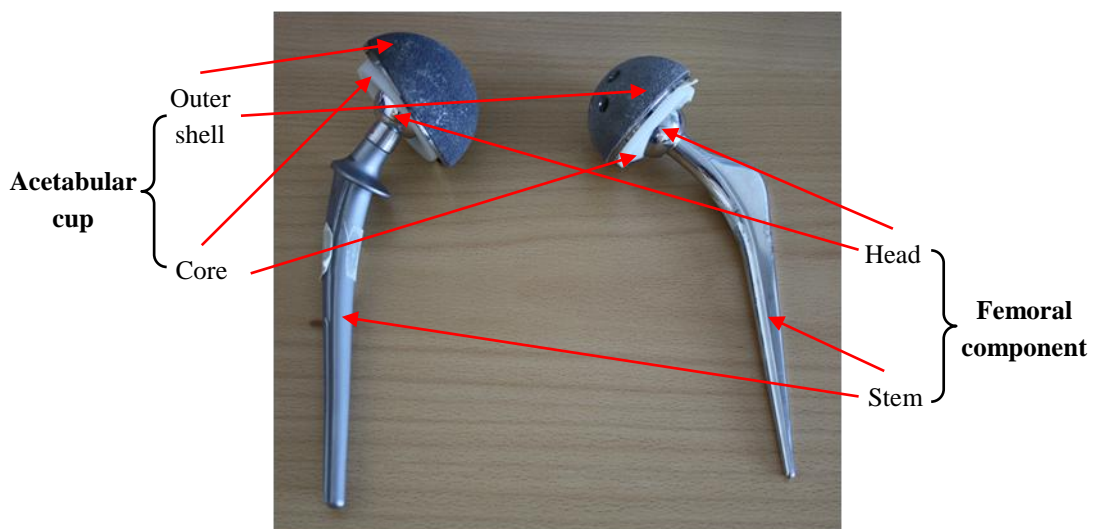


Figure 2.12. Example of 2 different hip prostheses. Courtesy of Tampere University Hospital.

From Figure 2.12 one observes the possible size and shape variations between the hip implants. Shape differences are especially prominent in the stem region of the prosthesis. Another observation would be that the implant related structures would vary in

shape and intensity on the individual CT slices of a pelvic scan. This is due to the composite nature and structure complexity of the hip prosthesis.

Before discussing the impact this metallic object can have on clinical CT images, it is necessary to present a pelvic scan of a patient with no metallic objects present in the anatomy (Figure 2.13).

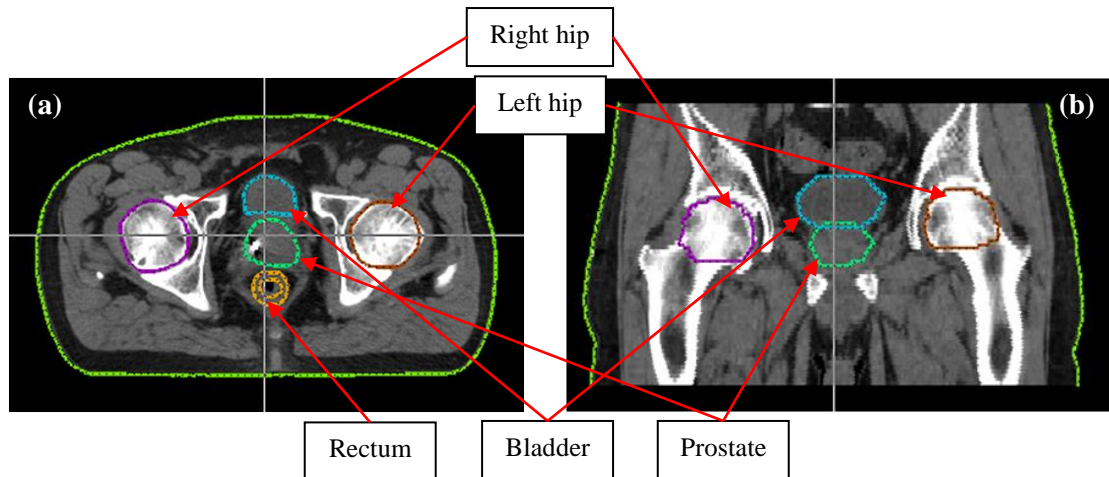


Figure 2.13. Example CT images from a hip prosthesis free male patient with key anatomical structures outlined by the radiation oncologist: axial (a) and coronal (b) views, respectively. The images are viewed with $WW = 500$ HU and $WL = 100$ HU. Courtesy of Tampere University Hospital.

The CT images provided in Figure 2.13 are rich in anatomical information with good tissue contrast and low noise levels. With this information at hand, a set of images describing the metal artifact corrupted pelvic CT scan with a single hip implant can now be introduced (Figure 2.14).

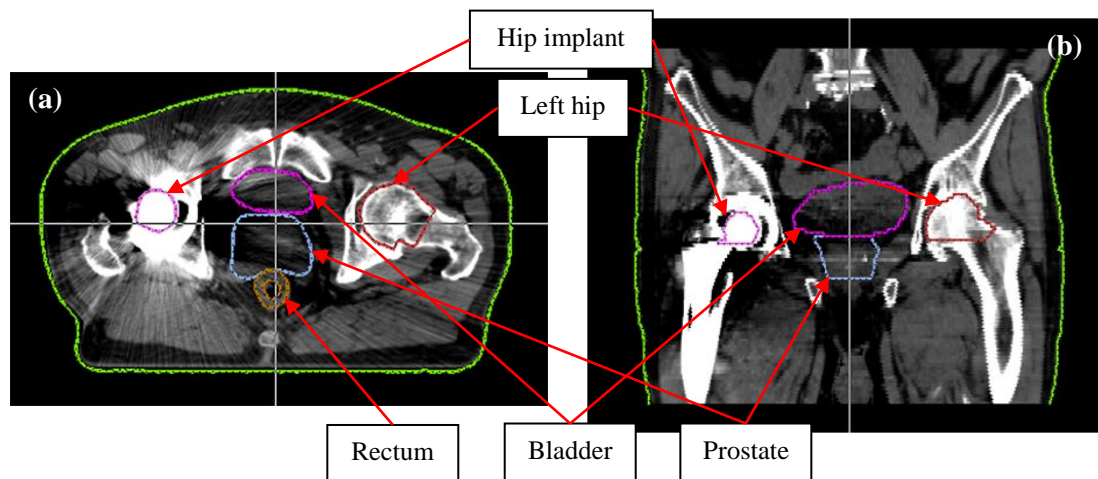


Figure 2.14. Example CT images from a male patient with a metallic hip implant and with key anatomical structures outlined by the radiation oncologist: axial (a) and coronal (b) views, respectively. Same display parameters as for Figure 2.13 are applied. Note the distortions introduced by the presence of the hip prosthesis. Courtesy of Tampere University Hospital.

When both hips contain metallic prostheses, artifact levels in the CT images are even more elevated (Figure 2.15).

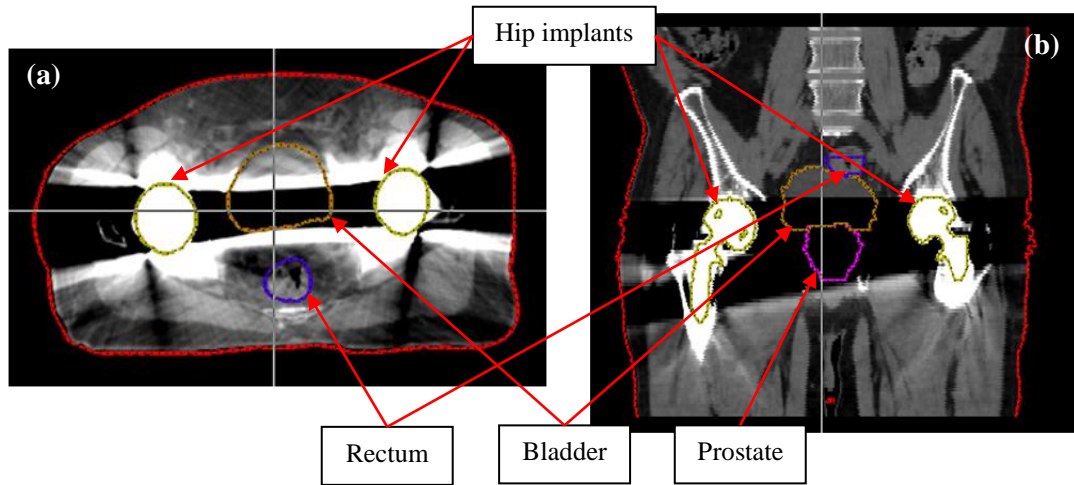


Figure 2.15. Example CT images from a male patient with two metallic hip implants and with key anatomical structures outlined by the radiation oncologist: axial (a) and coronal (b) views, respectively. Same display parameters as for Figure 2.13 apply. Images reflect an even more severe metal artifact caused by the prostheses compared to Figure 2.14. Courtesy of Tampere University Hospital.

From Figure 2.14 severe dark streaks along with thinner white streaks emanating from the metallic object can be observed. As for the two implants case (Figure 2.15), there are major dark streaks bordered by white streaks connecting the two metallic objects. They are a result of beam hardening, scatter and EEGE effects induced by the metal and are similar to the simulated ones provided in Figure 2.11. As a result, image intensities in these regions are either substantially lower or higher than normal. As seen from both axial and coronal views, the distortions produced by two hip prostheses are far more pronounced in comparison with the one implant case. Noise content in the images containing prostheses (Figures 2.14-2.15) is much more elevated, when compared to Figure 2.13. From the coronal view the dependence of the artifact on the implant structure and composition can be seen: the amount of lowered CT numbers is larger in the proximity of the acetabular cup and the upper part of the stem. This is especially visible in the images of the patient with a single hip prosthesis.

All of the outlined distortions caused by the presence of hip prosthesis in a pelvic CT scan impose difficulties in the use of such data in clinical practice.

2.2.2. Impact on radiotherapy treatment planning

Radiotherapy, also referred to as radiation therapy, radiation oncology or therapeutic radiology, is one of the three principal modalities responsible for the treatment of malignant disease (cancer), the other two being surgery and chemotherapy [5].

The main goal of radiotherapy is to eliminate or at least reduce the amount of malignant tissue present in the patient through ionizing radiation. Patient irradiation is

commonly performed by a linear accelerator (linac) producing a photon (x-rays) or electron beam. Before implementing such a procedure, a preliminary step is to simulate the irradiation by utilizing a treatment planning system (TPS). Typically this simulation is based on the acquired CT image dataset of the patient. [5]

Firstly, the CT scan is used as the primary set of patient data for treatment planning. The external patient contours are then extracted with the aid of an edge detection technique. The internal organ contours are also identified. Additional tools such as image fusion and co-registration with other tomographic modalities (such as MRI) are available to allow target visualization improvement. [14] With this information at hand, a virtual patient can be constructed for 3D treatment planning. The simulated patient is used to determine the radiation beam geometry, tumor localization, critical anatomical structures and to perform radiation dose calculations. In order to improve dose calculation accuracy, tissue inhomogeneity correction is applied. Tissue inhomogeneity is derived by converting the HU in each voxel of the image dataset into radiological parameters such as electron or material density. [5; 14] To establish the relationship between the CT number and the radiological parameter, a tissue characterization phantom is typically scanned. The phantom consists of inserts with known electron or material density. The inserts are embedded in a homogeneous medium. By measuring the HU values in the inserts, a conversion curve can be established to relate these values to the radiological parameter. [14]

The metal artifacts produced in CT images by high-Z materials, such as metal prostheses, can severely alter the image quality as previously observed in Figures 2.14-2.15. The distortions cause the structure contours to be compromised and induce inaccuracies in the CT numbers. This imposes problems with structure delineation and dose calculation inaccuracies in radiotherapy treatment planning. When generating a treatment plan with CT images corrupted by the metal artifact, the radiation oncologists have to either make educated guesses while contouring both tumour regions and critical structures (for example, bladder, prostate or rectum) or image the patient with another imaging modality (MRI) to obtain the necessary structural information. The artifact regions are also commonly overridden to an artificial electron density in order to account for tissue heterogeneities in the treatment planning process. [15] The metal structure HU values are also commonly higher than normal (Figures 2.14-2.15). This entails the necessity to separate the metallic objects from the rest of the image. Such an operation is best performed on the unrestricted HU scale described previously in Chapter 2.1.4.

One of the most frequent tumor cases is prostate cancer. It accounts for about 30% of male patients and about 15% of all cancer patients in Finland [16]. This entails an abundant number of cases treated by radiotherapy to be those with prostate cancer. Pelvic CT images, which can be severely compromised by the possible presence of a metallic hip prosthesis, are used in this case for treatment simulations. This provides another rationale for limiting this work to the hip implant metal artifact case.

2.3. Metal artifact reduction techniques

In the past three decades various approaches have been proposed for the reduction of the undesirable effects imposed by metallic implants on CT images. These approaches are generally referred to as *metal artifact reduction* (MAR) techniques. The majority of these proposed methods are mathematical algorithms that aim to correct the problem either iteratively or non-iteratively. [17]

Iterative techniques have the potential of correcting for distortions caused by metal objects by applying certain modifications at individual steps of the iterative reconstruction algorithm [15; 17; 18; 19]. Despite producing substantial improvements to the CT images corrupted by metal artifacts, these methods entail a high computational cost. Since the method to be presented in this work is based on non-iterative MAR techniques, iterative MAR methods will not be considered further, however, the reader is invited to experience the performance of such methods in the studies by Li et al. [15], Boas et al. [18], De Man et al. [19] and Zhang et al. [20].

The main concept behind non-iterative techniques for metal artifact correction is to detect projection domain samples affected by metallic objects and to replace them by appropriate estimates. This entails some form of interpolation. Hence these methods can also be referred to as *sinogram interpolation methods*. [17] Most of these techniques follow the same algorithm (Figure 2.16).

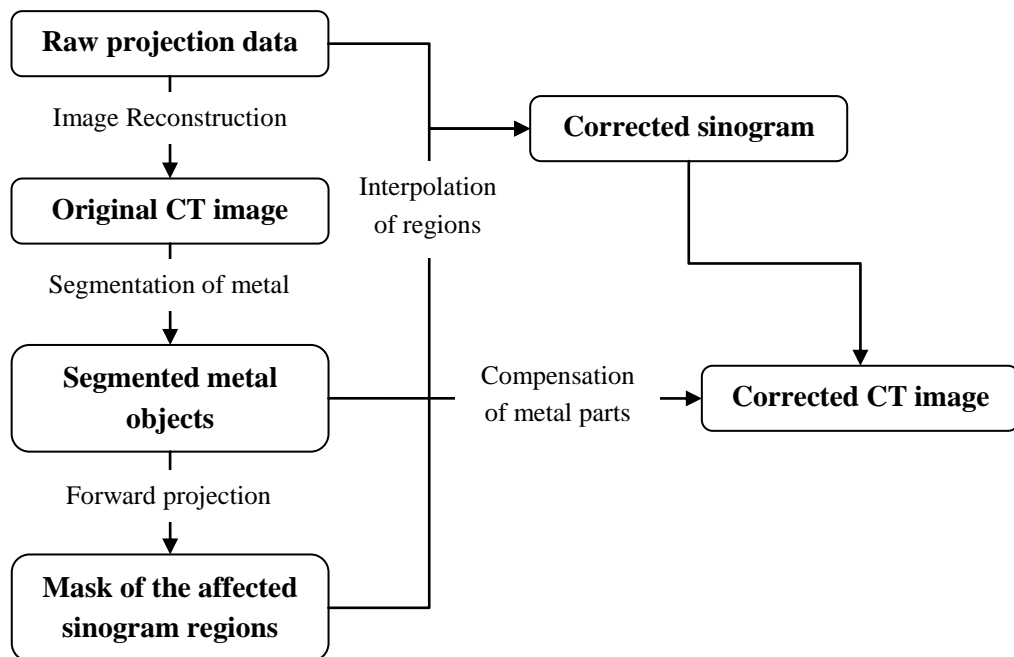


Figure 2.16. Overview of the basic steps constituting a sinogram interpolation MAR method.

In Figure 2.16 the term *forward projection* is used to describe the operation of the image-to-projection domain conversion. This conversion may not necessarily be carried out through parallel beam projection. Compensation of metal parts is usually performed

by replacing regions occupied by them in the corrected image with the ones extracted from the original.

Metal segmentation and sinogram interpolation play a key role in the performance of reduction methods summarized by Figure 2.16. These steps may vary significantly through the numerous implementations of non-iterative MAR techniques.

Metal object segmentation

The simplest approach to metal extraction is *global thresholding*. Consider a pixel $\mathbf{p} = [x, y]$. Then, given a grayscale image $I(\mathbf{p})$ and an *intensity threshold* I_t , the global thresholding operation $T\{\cdot\}$ can be defined as follows:

$$T\{I(\mathbf{p})\} = \begin{cases} 1, & I(\mathbf{p}) \geq I_t \\ 0, & I(\mathbf{p}) < I_t \end{cases} \quad (2.17)$$

From (2.17) it is straightforward to conclude that a product of a global thresholding operation on a grayscale image is a binary image. The thresholding approach can either be applied directly to the image under consideration [21; 22] or with an additional pre-processing to improve segmentation accuracy [23].

More elaborate approaches for metal extraction in sinogram interpolation MAR methods have also been proposed. Examples include segmentation based on mutual information [24] and compressed sensing theory [25].

Sinogram interpolation

Before describing the techniques implemented for projection data correction, it is worth mentioning that the term *inpainting* is often used instead of interpolation in the context of MAR methods.

A common solution for the sinogram interpolation problem is to implement linear interpolation (LI) [21; 23]. Although a simple solution, LI is computationally fast and provides good results in eliminating most distortions induced by the metals. The drawback of this method is the possible presence of new artifacts in the corrected image [25].

Partial differential equation (PDE) methods have also been applied to replace the compromised projection values. Such methods include, for example, total variation (TV) based inpainting [26] and fractional-order curvature driven diffusion (FCDD) [22]. Both TV and FCDD act as promising MAR techniques with performance superior to LI, but require more computational power due to the iterative process involved in solving PDEs, which serve as the basis for both models.

There are also some alternative mathematical methods to address the sinogram inpainting task. One example of such a technique is coherence transport inpainting. This method gives results similar to TV while being practically as fast as LI. However, it must be noted that the study was only concerned with assessing numerical phantom images and performance on clinical data is yet to be evaluated. [27]

Hybrid sinogram correction methods

An alternative category of metal artifact correction approaches should also be mentioned. They are partially based on non-iterative MAR methods and are called *hybrid sinogram correction methods*. [17]

Watzke et al. [28] proposed to combine the LI approach and multidimensional adaptive filtering (MAF) introduced by Kachelriess et al. [29]. MAF is applied on the projection data to reduce noise induced by metals in the CT images. This property is more pronounced at greater distances from the metallic object. LI, on the other hand, tends to introduce extra artifacts at these distances. With the aid of distance-directional weighting, the images resulting from both operations are superimposed to reduce metal artifact in terms of noise and streaking. [28] The method provides results comparable to those obtained with PDE techniques while being computationally fast.

Another prominent hybrid sinogram correction method is the Metal Deletion Technique (MDT). It iterates a modified version of the algorithm described in Figure 2.16 four times to obtain a final result. After performing metal segmentation and sinogram interpolation with LI, the MDT applies an edge preserving blur filter and forward projection to obtain a new estimate of the projection space. The corrupted values in the sinogram of the original image are then replaced with the values from the estimate and FBP is performed to reconstruct a corrected image. The final step is, as in Figure 2.16, to add the metallic objects to the corrected image. Despite the iterations characteristic to the MDT, it still runs fast because the number of iterations is low. The MAR performance of the algorithm is also noteworthy. [12; 18; 30] Results of MDT are superior to those provided by the pure non-iterative LI method and produce an improvement in disease diagnosis [6; 12].

The sinogram interpolation methods described in this chapter rely on the availability of raw projection data from the CT system. However, the data is often stored in a proprietary format. Therefore it is not always accessible. This obstacle can be overcome by forward projecting the reconstructed image. Unfortunately, such an operation provides only an approximation of the raw projection data. [6; 17; 30]

3. MATERIALS AND METHODS

With the theoretical framework supplied by Chapter 2, the methodology for reducing metal artifacts in pelvic CT scans can now be presented. Chapter 3.1 outlines the materials used in the study while Chapter 3.2 gives detailed description of the designed method.

Chapter 3.2 is further decomposed (Chapters 3.2.1-3.2.6) to explain the individual components of the proposed MAR technique. These include slice selection and processing (Chapters 3.2.1-3.2.2), metal object segmentation (Chapter 3.2.4), sinogram interpolation (Chapter 3.2.5) and channel weighting (Chapter 3.2.6).

3.1. Materials

The study was conducted at Tampere University Hospital. Two CT image datasets were used to test the performance of the MAR algorithm: patients with one and two hip implants, respectively. All the uncorrected CT images with metal artifacts presented within the following chapter are courtesy of Tampere University Hospital.

Images were acquired using a 16 slice helical CT scanner (Aquilion LB, Toshiba Medical Systems Corporation, Otawara-shi, Japan). The reconstruction scheme applied in the scanner is based on the Feldkamp-Davis-Kress (FDK) algorithm. The following tube setting was used for the one hip prosthesis case: exposure of 440 milliamperes (mAs) and 120 peak kilovoltage (kVp). The two hip implant patient scan was obtained with the same kVp, but an exposure of 330 mAs. The CT image datasets were saved in a standard Digital Image and Communications in Medicine (DICOM) format with sizes of 512x512x102 px and 512x512x119 px for the one and two implant cases, respectively. Pixel size was 1.002 mm and 1.110 mm for the one and two hip prostheses scans, respectively. Reconstructed image slice thickness was 3.000 mm for both datasets. The intensity information in each pixel was stored with 16 bits (65536 possible gray levels) in both cases. Intensity value offset for both datasets was equal to 1000.

The metal artifact correction algorithm was implemented in MATLAB (Windows version 7.12.0, The MathWorks Inc., Natick, Massachusetts, USA) environment. CERR (version 4.1, Advanced Radiotherapy Treatment Planning Group, Memorial Sloan-Kettering Cancer Center, New York, USA) was used to import images into MATLAB and to visualize them before and after applying the designed MAR method. Quantitative measurements were carried out with the aid of Eclipse treatment planning software (Varian Medical Systems, Palo Alto, California, USA). The algorithm was executed on a laptop computer with a 2.2 GHz dual core processor, 4 GB of RAM and 32-bit Windows 7 operating system.

3.2. Channel Fusion Metal Artifact Reduction

A novel non-iterative hybrid sinogram interpolation MAR method has been developed to combat the metal artifact characteristic to pelvic CT scans with hip prostheses described in Chapter 2.2.1 (Figures 2.14-2.15). It is loosely based on the work of Watzke et al. [28]. The used algorithm is composed of two essential phases (Figure 3.1): detect slices with metal objects in the image dataset supplied by CERR (preliminary step) and reduction of the metal induced distortion on every detected slice (the application of the MAR technique).

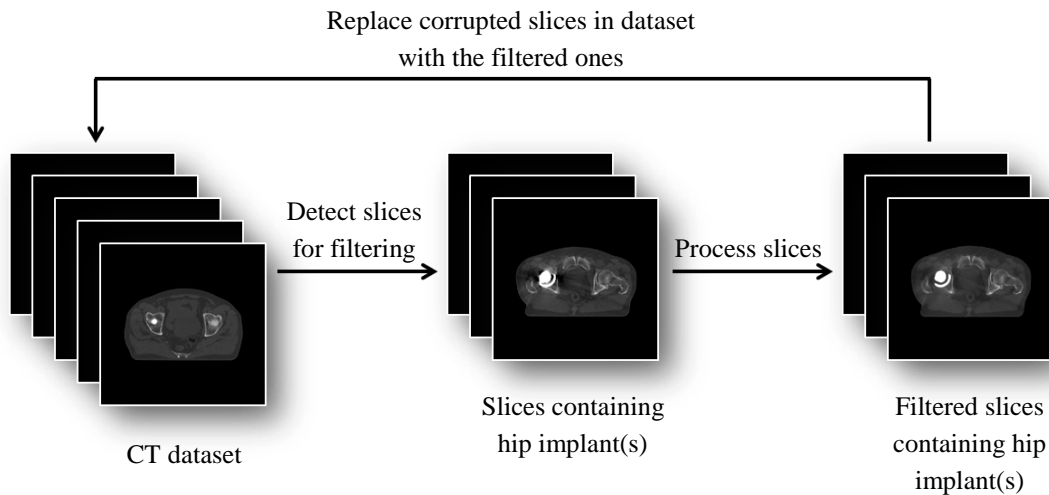


Figure 3.1. General overview of the algorithm application to a given CT dataset

The slice selection approach outlined in Figure 3.1 avoids processing of extra CT slices. This entails a speed-up in the overall performance of the method on a specified pelvic CT dataset.

3.2.1. Slice detection

Because, usually, not all of the images from a given pelvic CT scan have metal present, it is necessary to separate those that do from the overall dataset (Figure 3.1). This is done by computing the maximum HU value for every slice in the scan. Thereafter, every slice with a maximum HU value greater than a certain user defined HU value is classified as one containing metal. The value can be chosen based on the upper limit of the CT number scale for anatomical tissue (Chapter 2.1.4, Table 2.1).

The slice detection phase of the algorithm also incorporates the determination whether the patient has single or multiple prostheses. This is done by summing the intensities in the columns of the central slice from the segment of the dataset containing metal. Then maxima on either side from the centre of the resulting 1D profile are computed. In the case of one hip implant the maxima will exhibit a large difference. The largest maximum in this case also defines in which hip the implant is located.

A schematic representation of the implant case detection is provided in Figure 3.2.

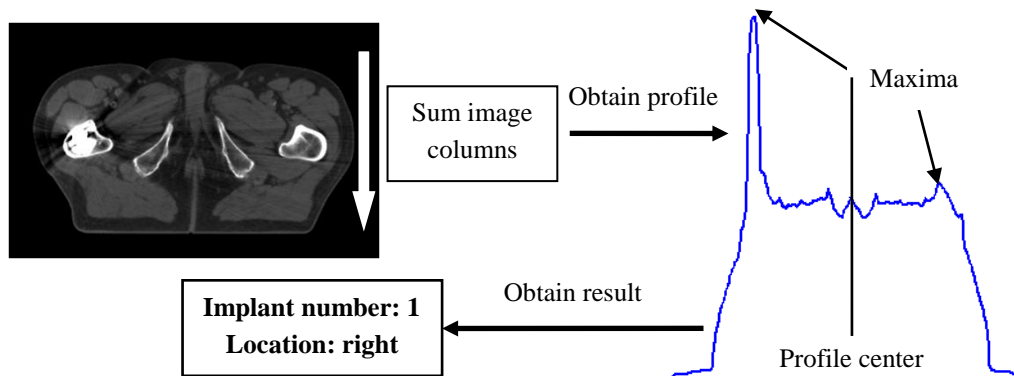


Figure 3.2. Illustration of hip prosthesis number and location determination.

From Figure 3.2 one notes that in the case of a double hip implant patient the difference between the profile maxima would not be as prominent. Hence, such a case can be easily differentiated from the single hip prosthesis case with the proposed approach.

3.2.2. Slice processing

Once the CT images containing metal objects have been extracted from the dataset and the number and location of metal hip prostheses has been determined, the actual MAR can be initiated (Figure 3.3).

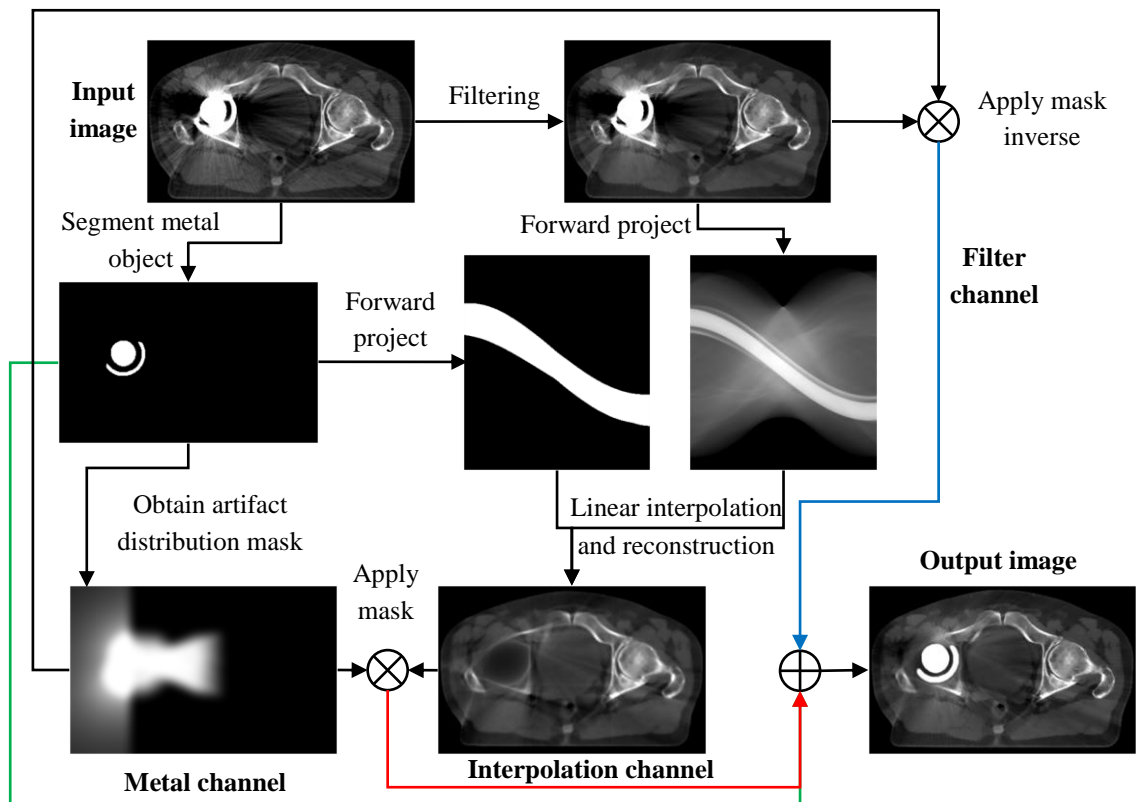


Figure 3.3. Schematic of the designed metal artifact reduction method.

Figure 3.3 describes the main idea behind the MAR method. Firstly, filtering is applied on the input CT intensity image $I(\mathbf{p})$ to produce a filtered version $I_{GBF}(\mathbf{p})$. Then, the sinogram of $I_{GBF}(\mathbf{p})$ is computed via the parallel beam representation of the RT. Metal regions are extracted to create a metal mask $M(\mathbf{p})$. The RT is also applied to the segmented metal objects to identify the region of interpolation in the projection domain of $I_{GBF}(\mathbf{p})$. Utilizing this information, LI is performed, and an estimate image $I_{LI}(\mathbf{p})$ is reconstructed via FBP with a Hamming filter. The extracted metallic parts of the image also serve the purpose of constructing the artifact distribution mask $W(\mathbf{p})$. Finally, the metal artifact reduced image $I_{MAR}(\mathbf{p})$ is obtained by combining $I_{GBF}(\mathbf{p})$, $I_{LI}(\mathbf{p})$, $W(\mathbf{p})$ and $M(\mathbf{p})$, in the following manner:

$$I_{MAR}(\mathbf{p}) = I_{GBF}(\mathbf{p})(1 - W(\mathbf{p}) - M(\mathbf{p})) + I_{LI}(\mathbf{p})(W(\mathbf{p}) - M(\mathbf{p})) + C_M M(\mathbf{p}), \quad (3.1)$$

where C_M value to be assigned to the metal regions by the user.

Every member in the sum provided by (3.1) is denoted as a *channel* in Figure 3.3. Members containing $I_{GBF}(\mathbf{p})$, $I_{LI}(\mathbf{p})$ and $M(\mathbf{p})$ are called *filtering*, *interpolation* and *metal channels*, respectively. To produce $I_{MAR}(\mathbf{p})$, the channels are *fused*. Thus, the designed metal artifact correction method is given the name *Channel Fusion Metal Artifact Reduction* (CFMAR).

The idea is to take the regions mostly affected by the streak component of the metal artifact from $I_{LI}(\mathbf{p})$ and to take the rest from $I_{GBF}(\mathbf{p})$. Such a strategy minimizes the inclusion of artifacts produced in the image obtained from a linearly interpolated sinogram. Because metal values tend to be excessively high, the metal is excluded from both images and added to the final image with the value specified by C_M . This value is supplied by the user.

The introduced algorithm differs from the one introduced by Watzke et al. [28] in some key aspects. MAF filtering is replaced by edge preserving spatial filtering examined in Chapter 3.2.3. Instead of hard thresholding, segmentation of metal parts is done via intelligent thresholding discussed in more detail in Chapter 3.2.4. The artifact distribution mask is constructed using a different approach which is explained in more detail Chapter 3.2.6. The only direct similarity is the application of LI to the sinogram interpolation problem (Chapter 3.2.5).

3.2.3. Filtering

In order to de-noise the CT images corrupted by the metal artifact, a modified version of the well known *bilateral filter* (BF) is implemented. The filter performs Gaussian smoothing selectively on the intensity image under consideration: smooth only the flat regions [31]. To provide an understanding of bilateral filtering some key notation will be introduced.

Consider again the grayscale image $I(\mathbf{p})$. The Gaussian low-pass filtering operation (or Gaussian blur) $GB\{\cdot\}$ on this image can be defined in the following manner [32; 33]:

$$I_{GB}(\mathbf{p}) = GB\{I(\mathbf{p})\} = \sum_{\mathbf{q} \in S} G_{\sigma}(\mathbf{p} - \mathbf{q})I(\mathbf{q}), \quad (3.2)$$

where $I_{GB}(\mathbf{p})$ is the Gaussian filtered image, $G_{\sigma}(\mathbf{p} - \mathbf{q})$ is a 2D Gaussian kernel centred at pixel \mathbf{p} , S is a local neighbourhood around that pixel and \mathbf{q} is a pixel from S . The Gaussian kernel from (3.2) has the form:

$$G_{\sigma}(\mathbf{p} - \mathbf{q}) = \frac{1}{2\pi\sigma} e^{-\frac{\|\mathbf{p}-\mathbf{q}\|^2}{2\sigma^2}}, \quad (3.3)$$

where σ is the standard deviation and $\|\cdot\|$ is the Euclidean distance.

Thus, Gaussian filtering is a weighted average of the pixel intensity values around a center pixel \mathbf{p} with the weights being specified by $G_{\sigma}(\mathbf{p} - \mathbf{q})$. This causes image blurring and does not preserve any edges. The parameter σ determines the spread of the Gaussian kernel defined in (3.3). A larger σ implies a higher level of blurring [32; 33].

The BF introduces an intensity dependent component in the operation introduced in (3.2) and is formulated as follows [31; 32]:

$$I_{BF}(\mathbf{p}) = BF\{I(\mathbf{p})\} = \frac{1}{C_{\mathbf{p}}} \sum_{\mathbf{q} \in S} G_{\sigma_s}(\mathbf{p} - \mathbf{q})G_{\sigma_r}(I(\mathbf{p}) - I(\mathbf{q}))I(\mathbf{q}), \quad (3.4)$$

where $I_{BF}(\mathbf{p})$ is the filtered image, $BF\{\cdot\}$ is the bilateral filtering operation and G_{σ_s} and G_{σ_r} are 2D *spatial* and *range* Gaussian kernels with the spreads equal to σ_s and σ_r , respectively. The parameter $C_{\mathbf{p}}$ is a normalization factor of the following form [31; 32]:

$$C_{\mathbf{p}} = \sum_{\mathbf{q} \in S} G_{\sigma_s}(\mathbf{p} - \mathbf{q})G_{\sigma_r}(I(\mathbf{p}) - I(\mathbf{q})) \quad (3.5)$$

The new term G_{σ_r} is essential to limit the 2D Gaussian blurring based on the intensity (or range) differences of the pixels in the neighbourhood of the central pixel \mathbf{p} . Thus, the influence of pixels \mathbf{q} with an intensity value different from the value at \mathbf{p} will be low. The difference is controlled by σ_r . This provides an edge preserving effect. A demonstration of bilateral filtering is given in Figure 3.4.

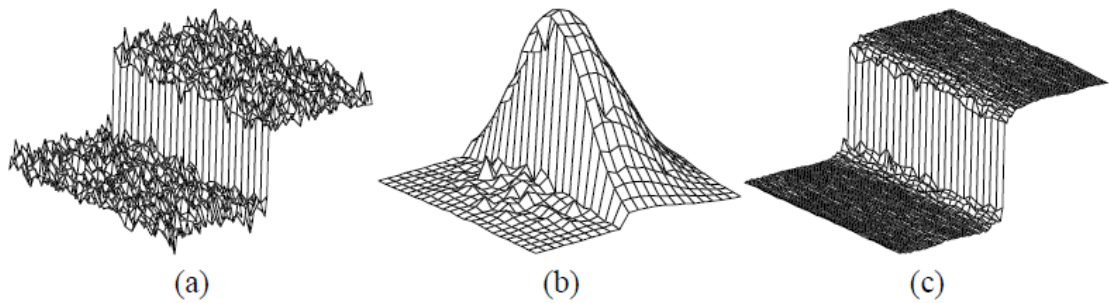


Figure 3.4. Illustration of bilateral filtering performed on a step edge corrupted by additive Gaussian noise (a). Filter kernel is depicted centred a few pixels away on the top part of the edge (b). The range component suppresses smoothing across the edge. The result of filter application is shown in (c). [31] Adapted from Tomasi et al. [31].

The BF becomes closer to a Gaussian blur of (3.2) as the range spread parameter σ_r increases because the range kernel gets closer to a constant. The increase of σ_s provides a larger scale of blurring.

An important characteristic of the filtering operation defined in (3.4) is the weight multiplication. This implies that as soon as one of the weights is close to 0, no smoothing is performed. Thus, a spatial Gaussian with a large spread coupled with a narrow spread range Gaussian achieves limited smoothing and vice versa.

Although the BF operation preserves edges, the preservation is not perfect and some edges are sharpened during the process. This introduces an undesirable *staircase effect*. Thus, artificial contours can be created and consistency of the existing ones may be altered. [32; 34] To elude this effect, the BF is modified. After applying (3.4), the gradient magnitude is computed for both the resulting and the original unfiltered images, respectively. The pixels in $I_{BF}(\mathbf{p})$ are replaced by the corresponding pixels in $I(\mathbf{p})$ if their gradient magnitude is higher:

$$I_{GBF}(\mathbf{p}) = GBF\{I(\mathbf{p})\} = \begin{cases} I_{BF}(\mathbf{p}), & \|\nabla I_{BF}(\mathbf{p})\| \leq \|\nabla I(\mathbf{p})\| \\ I(\mathbf{p}), & \text{otherwise} \end{cases} \quad (3.6)$$

Here $I_{GBF}(\mathbf{p})$ denotes the image obtained after applying the gradient modified bilateral filter (GBF), $GBF\{\cdot\}$ is the respective filtering operation and ∇ is the gradient operator defined as follows:

$$\nabla I(\mathbf{p}) = \left[\frac{\partial I(\mathbf{p})}{\partial x}, \frac{\partial I(\mathbf{p})}{\partial y} \right] \quad (3.7)$$

From (3.6) one notes that the imposed modification prevents an increase in gradient magnitude, thus, avoiding the sharpening of edges and inclusions of new contours.

For the CFMAR filter kernel size and the spatial spread σ_s are fixed to 13x13 px and 3 px, respectively. The range parameter σ_r is user chosen, thus, allowing the user to control the GBF effect on the given CT dataset. Finally, an example of the implemented de-noising filter application on a CT intensity image corrupted by the metal artifact is supplied in Figure 3.5.

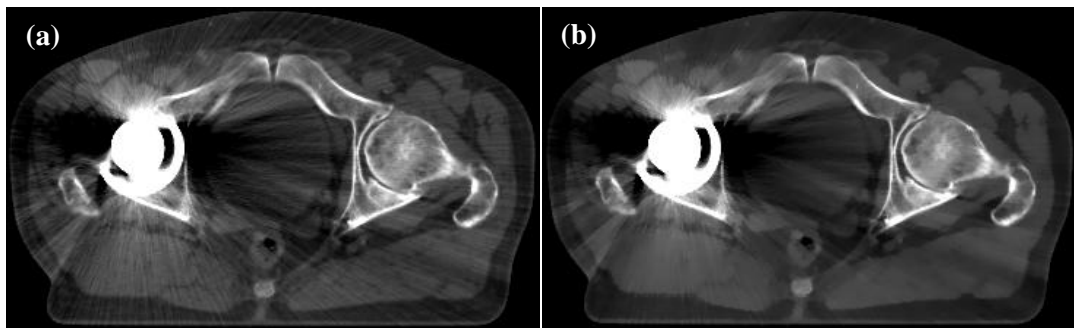


Figure 3.5. A metal artifact corrupted CT image (a), and the same image after applying the gradient modified bilateral filter (b).

Figure 3.5 shows how anatomical tissue contours are being preserved while the image noise is being reduced upon GBF application. The de-noising effect of the designed filter is especially noticeable in muscle tissue regions.

3.2.4. Metal segmentation

Because of the edge effects caused by metal (Chapter 2.2, Figure 2.11), a simple hard thresholding operation might not present the optimum solution to the segmentation problem. To separate the metals from the rest of the CT image, an intelligent thresholding approach with object labelling based on pixel 8-connectivity is employed. The objects are separated into those that are related to the implant and those that are not. The latter objects are usually metallic seeds implanted in the prostate. The extraction of seed objects is necessary because of their role in patient positioning during a radiotherapy treatment and CT-MRI image co-registration. The separation is done based on the number of pixels within an object.

The segmentation part of the CFMAR requires a minimum metal threshold from the user. A good choice would be 2500-3000 HU. Based on the minimum threshold a second higher threshold value is computed utilizing the image intensity distribution $H(i)$ which does not include values lower than the user specified threshold. The intensity distribution is called a *histogram* and is defined in terms of the grayscale image $I(\mathbf{p})$ and image intensity i :

$$H(i) = \sum_{\mathbf{p}} \delta(I(\mathbf{p}) - i) \quad (3.8)$$

Two binary images $M_l(\mathbf{p})$ and $M_h(\mathbf{p})$ are then created by thresholding $I(\mathbf{p})$ with both *low* and *high thresholds*, respectively. Objects are created based on pixel *8-connectivity* which, for a binary image, is defined as follows [33]: a non-zero pixel \mathbf{q} is 8-connected to a non-zero pixel \mathbf{p} , if \mathbf{q} lies in the immediate neighbourhood of \mathbf{p} . This is also true if \mathbf{p} lies in the neighbourhood of \mathbf{q} . Figure 3.6 illustrates the 8-connectivity statement.

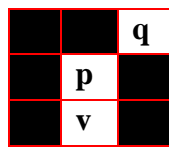


Figure 3.6. Immediate neighbourhood of a pixel \mathbf{p} with pixels \mathbf{q} and \mathbf{v} . White color represents non-zero pixels (value 1) and black – zero valued pixels. Thus, \mathbf{q} and \mathbf{v} are 8-connected to \mathbf{p} .

As noted earlier, seeds are separated from $M_l(\mathbf{p})$ based on pixel number within an object. They are also removed from $M_h(\mathbf{p})$. Now the binary images only contain hip prosthesis related regions. The low threshold is then linearly increased towards the high threshold until the number of objects in $M_l(\mathbf{p})$ is the same as in $M_h(\mathbf{p})$. This is necessary because the regions in $M_h(\mathbf{p})$ do not cover all the metal pixels from the image undergoing segmentation, however, merging of unconnected objects and excessive pixel inclusion characteristic to the initial $M_l(\mathbf{p})$ is avoided. Thus, $M_h(\mathbf{p})$ serves the purpose

of estimating the number of hip implant related regions. The concept of intelligent thresholding is depicted in Figure 3.7.

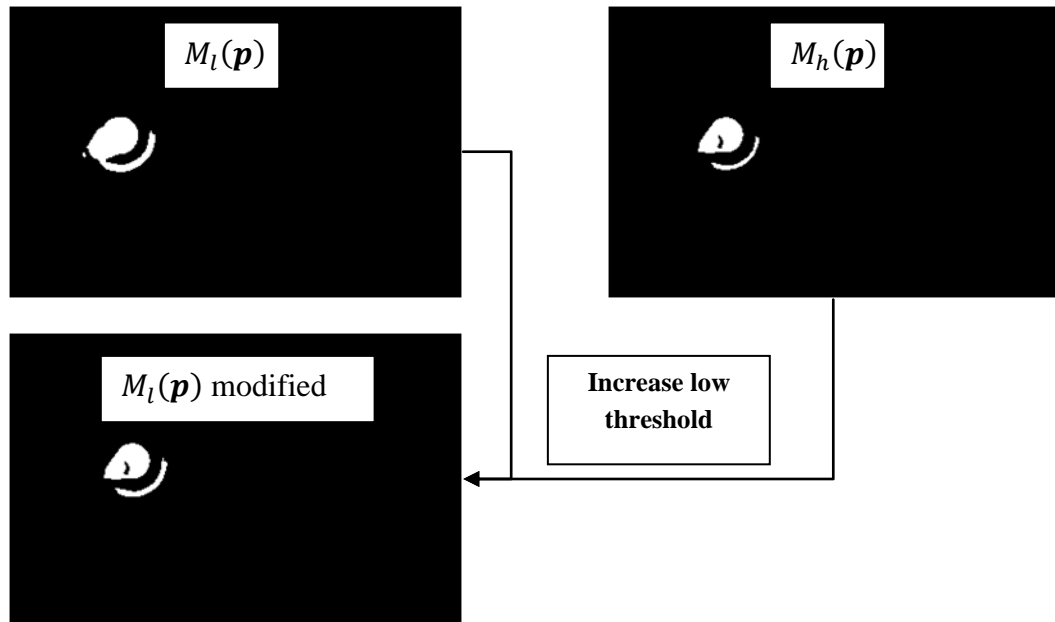


Figure 3.7. Schematic representation of intelligent thresholding. Note in the beginning $M_l(\mathbf{p})$ exhibits one major object. After the threshold modification the object is separated into two.

The final step is to add the seeds back to the modified $M_l(\mathbf{p})$ and to smooth the result with a Gaussian kernel obtaining $M(\mathbf{p})$. The former operation avoids sharp changes between the metal and the rest of the image in the final metal artifact reduced image.

3.2.5. Sinogram interpolation

Once the segmentation of metal objects has been successfully performed, $M(\mathbf{p})$ can be used to estimate the regions in the sinogram of $I(\mathbf{p})$ (Figure 3.8a) related to these objects. This is done through the RT.

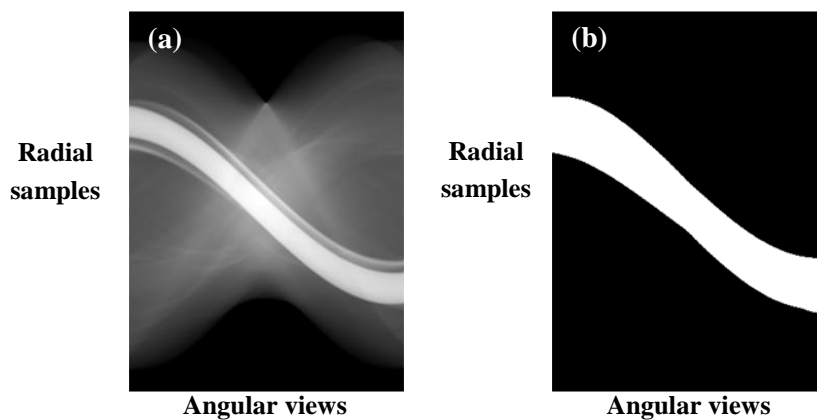


Figure 3.8. Projection domain representation of $I(\mathbf{p})$ (a) and the projection domain mask obtained from $M(\mathbf{p})$ (b). Note the high intensity metal traces visible in the image on the left.

The obtained metal sinogram is converted to a binary mask by setting all non-zero projection values to 1 (Figure 3.8b).

It is now necessary to perform LI in the regions specified by the mask in Figure 3.8. Taking into account the projection vector representation of the sinogram provided in Chapter 2.1.2 (Figure 2.3), one can conclude that these regions can produce a set of L intervals $\varepsilon_{Metal} = [\varepsilon_{\varphi,l}, \varepsilon_{\varphi,l} + \Delta\varepsilon_{\varphi,l}]$, $l = 1, \dots, L$ in a given projection vector taken at angle φ . L corresponds to the number of metal intervals. A data point (ε, φ) , $\varepsilon \in \varepsilon_{Metal}$ from an arbitrary interval l can be linearly interpolated in the following manner [28]:

$$p_{LI}(\varepsilon, \varphi) = p(\varepsilon_{\varphi,l}, \varphi) + \frac{p(\varepsilon_{\varphi,l} + \Delta\varepsilon_{\varphi,l}, \varphi) - p(\varepsilon_{\varphi,l}, \varphi)}{\Delta\varepsilon_{\varphi,l}} (\varepsilon - \varepsilon_{\varphi,l}), \quad (3.9)$$

where $\varepsilon_{\varphi,l}$ and $\Delta\varepsilon_{\varphi,l}$ represent the start point and the width of the interval l . It is straightforward to see that in the simplest case one deals with a single metal interval for each projection vector similar to the illustration in Figure 3.8.

Applying (3.9) to all L intervals for every projection vector from the sinogram of $I(\mathbf{p})$, one arrives at the following interpolated sinogram (Figure 3.9a). Finally, FBP reconstruction with Hamming filter is performed (Figure 3.9b).

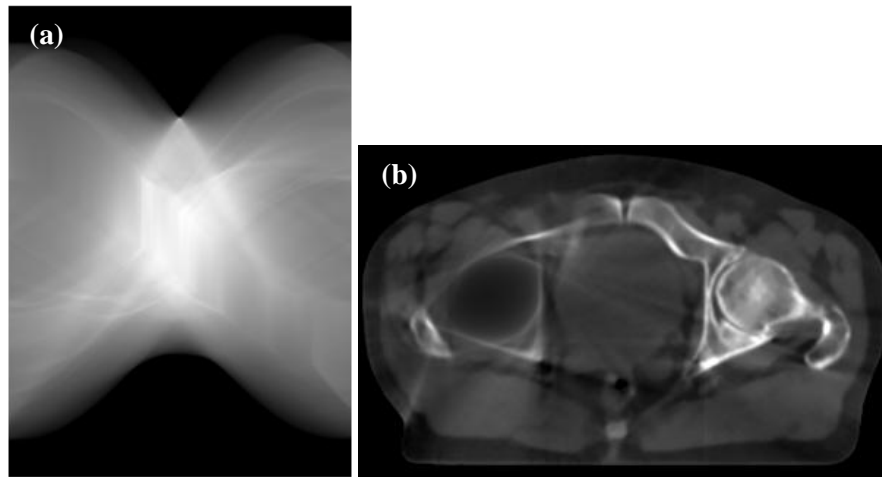


Figure 3.9. Sinogram of $I(\mathbf{p})$ after LI (a) and the resultant image reconstructed by FBP (b).

From the observation of the example image obtained after LI (Figure 3.9b), one notes the presence of artifacts. This illustrates the necessity of channel weighting in order to avoid these distortions.

3.2.6. Channel weighting

With all the necessary individual components for the channel fusion employed by CFMAR described, the only point left to clarify is the artifact distribution mask $W(\mathbf{p})$ (or simply channel weight mask) that, in combination with $M(\mathbf{p})$, produces channel weighting. To construct this mask, one employs an approach distantly similar to the one discussed in the work by Watzke et al. [28].

The sinogram of the metal objects is cubic weighted to emphasize the rays passing through a higher number of metal pixels. This is where the similarity with the technique designed by Watzke et al. [28] ends. The simple BP and exponential scaling proposed in that study to construct the mask from the enhanced metal sinogram do not quite mimic the distribution of the metal artifact in the CT image. Moreover, the resulting mask results in excessive information inclusion from the interpolation channel.

As noted previously in Chapter 2.2.1, the metal distortion in the image is slice dependent. With this observation at hand, two bases for the channel weight mask were applied for the one implant case. In the case of the acetabular cup and the femoral component, BP and FBP with Hamming filter from the modified metal sinogram were used, respectively. Thereafter, the masks were enhanced by using prior anatomical information to minimize the covering of bone structures around the metal and to provide better coverage of the streak artifact region. As a result, more information is taken from the interpolation channel in the regions contaminated with streaking whilst preserving the bone from the filtering channel.

In the case of two implants the dominant artifact distribution was mimicked by simply applying FBP with the Hamming filter to the cubic enhanced metal sinogram. As seen from Figure 2.15 (Chapter 2.2.1), the metal artifact is primarily distributed between the two hip prostheses along the column direction of the image. If additional streak artifacts were present, the algorithm would detect them and modify the weight mask accordingly.

An illustration of channel weight masks for the one and two hip implant cases is provided in Figure 3.10.

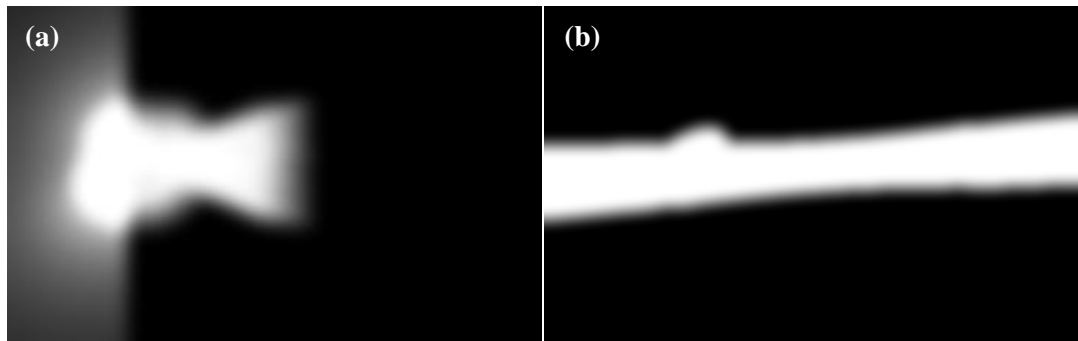


Figure 3.10. Example channel weight masks for the CFMAR in the case of single (a) and double (b) hip prosthesis.

The distribution mask in the single hip implant case (Figure 3.10a) exhibits a higher degree of complexity than in the double implant case (Figure 3.10b). When comparing these masks to Figures 2.14-2.15, one notes the pronounced amount of streak artifact coverage.

3.3. CFMAR performance analysis

The performance of the presented MAR algorithm was assessed both qualitatively and quantitatively on both one and two metallic hip implant cases. For this purpose, the following algorithm parameters were selected for the studied hip implant cases Table 3.1.

Table 3.1. CFMAR parameters applied for the examined hip implant cases.

| Algorithm parameter | Value in single implant case, HU | Value in double implant case, HU |
|------------------------------|----------------------------------|----------------------------------|
| Slice detection threshold | +3000 | +3000 |
| Segmentation threshold | +2400 | +2400 |
| Metal object value, C_M | +3500 | +3500 |
| GBF range spread, σ_r | +40 | +20 |

The qualitative assessment consisted of visual analysis of certain corrected images and their regions (sub-images). The quality of noise reduction, metal object segmentation and streak artifact reduction was addressed through the evaluation of these sub-images. Additionally, surface rendering of the implant structure was performed to assess segmentation accuracy.

Apart from the visual assessment of the CFMAR, it was necessary to perform some form of numerical measurements to evaluate the differences between the uncorrected and corrected CT images. For this purpose, the mean HU values with their corresponding standard deviations were measured within a homogeneous *region of interest* (ROI) for soft and fat tissue (Figure 3.11). These parameters serve as an indicator of overall MAR performance in terms of streak artifact component reduction of the metal artifact.

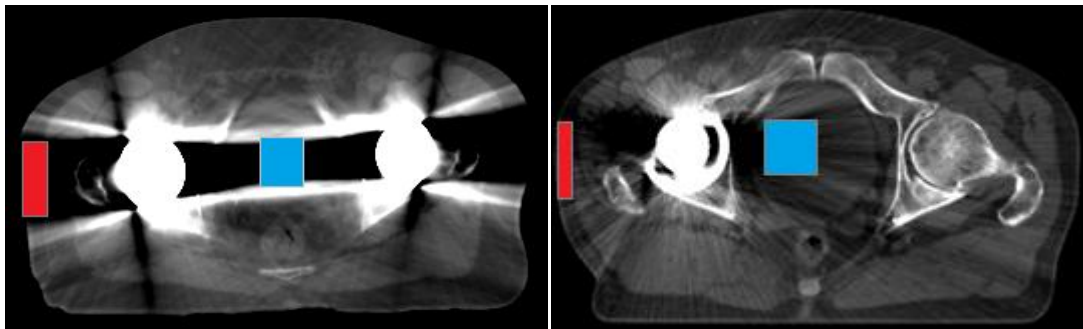


Figure 3.11. ROI locations for testing the performance of the CFMAR in the single (a) and double (b) hip prosthesis cases. The regions measuring statistics from soft tissue and fat tissue are depicted in red and blue, respectively. Note that the ROIs are positioned in the image sections corrupted by the metal artifact.

Finally, the computation time necessary for the CFMAR to perform artifact reduction was also assessed by running the algorithm 10 times on both hip prostheses cases and computing the mean values with the respective standard deviation. One notes that the purpose of this is to provide an overview of the possible run-time of the algorithm.

4. RESULTS

For qualitative evaluation of MAR efficiency three axial slice images and one coronal slice image were examined in both studied hip prostheses cases. One of the axial slice images from each case was decomposed into 5 sub-images to assess the efficiency of individual CFMAR components: de-noising (2 sub-images), metal region extraction (1 sub-image) and reduction of metal induced streaking (2 sub-images). To further evaluate segmentation accuracy, the implant structure before and after processing was rendered.

To quantify the MAR capability of the designed algorithm, 15 axial slice images from both single and double implant cases were subjected to the intensity statistics measurements explained in Chapter 3.3. Images were selected to include most part of the acetabular cup component and a fraction from the femoral component of the hip implant. The rationale behind this was twofold. Firstly, the metal artifact is less prominent for the stem component due to the significant object cross-section area decrease compared to the cup component. Secondly, it becomes increasingly problematic to obtain a homogeneous region within the area of artifact distribution for soft tissue measurements because this area begins to occupy less space in the image. For intensity measurements, the ROI size for fat tissue was set to 10x30 px. In the case of soft tissue, the applied sizes were 30x30 px and 25x25 px depending on the slice. The different sizes for soft tissue ROIs were due to the reduced area of the homogeneous regions in the femoral section of the pelvic CT scan.

All unfiltered CT images presented in Chapter 4.1 are courtesy of Tampere University Hospital.

4.1. Qualitative Evaluation

In the current chapter axial slice images and a coronal slice image from both datasets are presented before and after the application of CFMAR algorithm. The number of CT slices classified to have metal present was 60 and 65 for the single and double hip prostheses cases, respectively. The display parameters for all images presented in this chapter are: window width – 1000 HU and window level – 250 HU.

Figure 4.1 depicts three axial slice images from the pelvic CT scan of the patient with one metallic hip implant before and after applying the MAR algorithm.

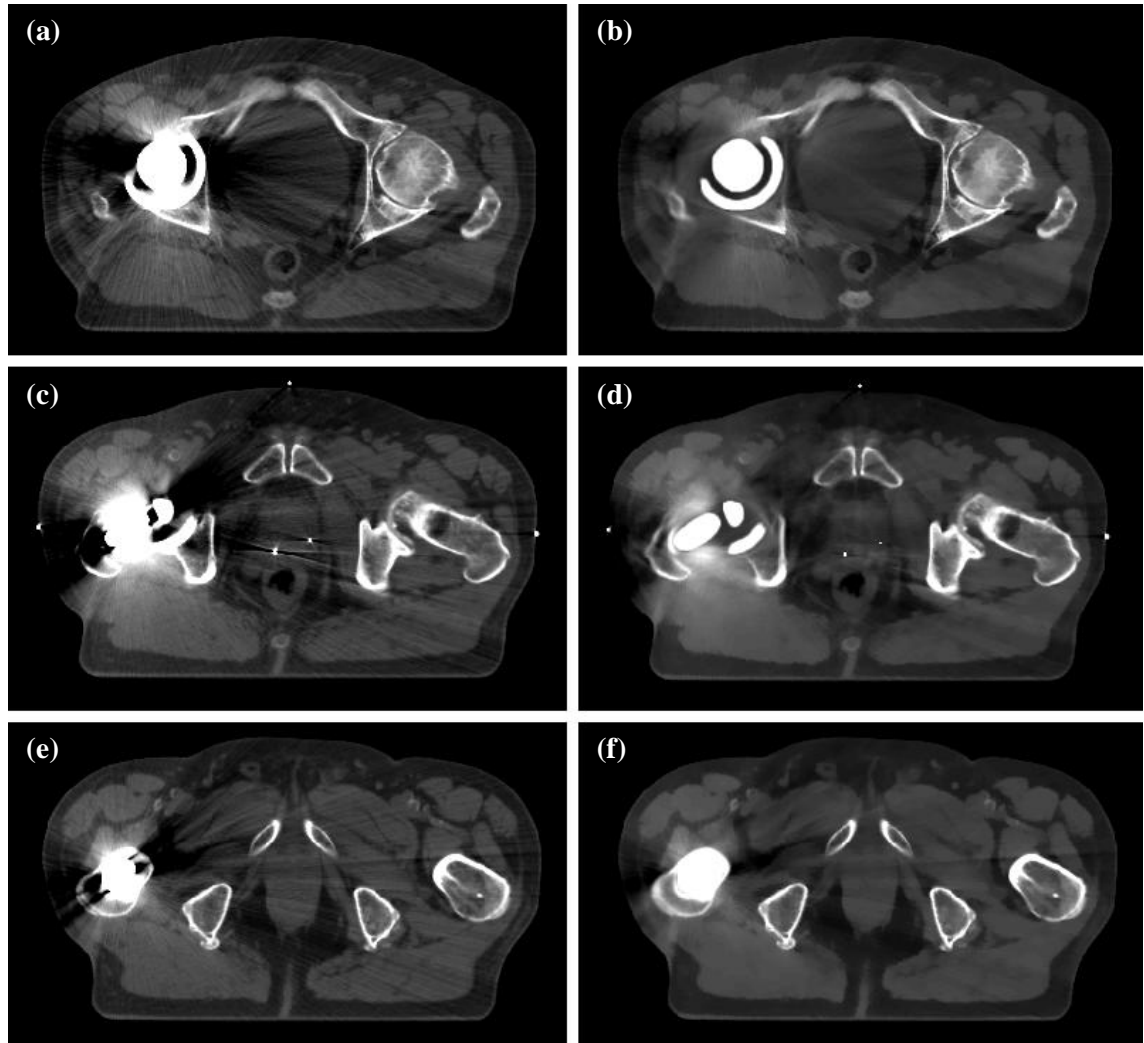


Figure 4.1. CT slice images obtained from the examined single hip prosthesis patient before (left column) and after (right column) CFMAR algorithm application. Top row, middle row and bottom row images depict axial slices of the acetabular cup, transitional and stem section of the metallic hip implant. The transitional section is where both parts of the stem and the cup components of the implant are present.

The observation of the CT images from Figure 4.1 shows a substantial reduction of streak component of the metal artifact as well as the EECE effect visible in the vicinity of metallic parts. The noise content is also reduced, however, at the expense of some

fine anatomical detail, especially in the muscle tissue regions. It is also worth noting that metallic objects become more discernible with the exception of Figure 4.1f. Finally, the image in Figure 4.1b depicts how the bladder contour in the area corrupted by the metal artifact is restored after CFMAR has been performed.

An analogous demonstration of the designed MAR method performance in the case of CT images containing two metallic hip prostheses is provided in Figure 4.2.

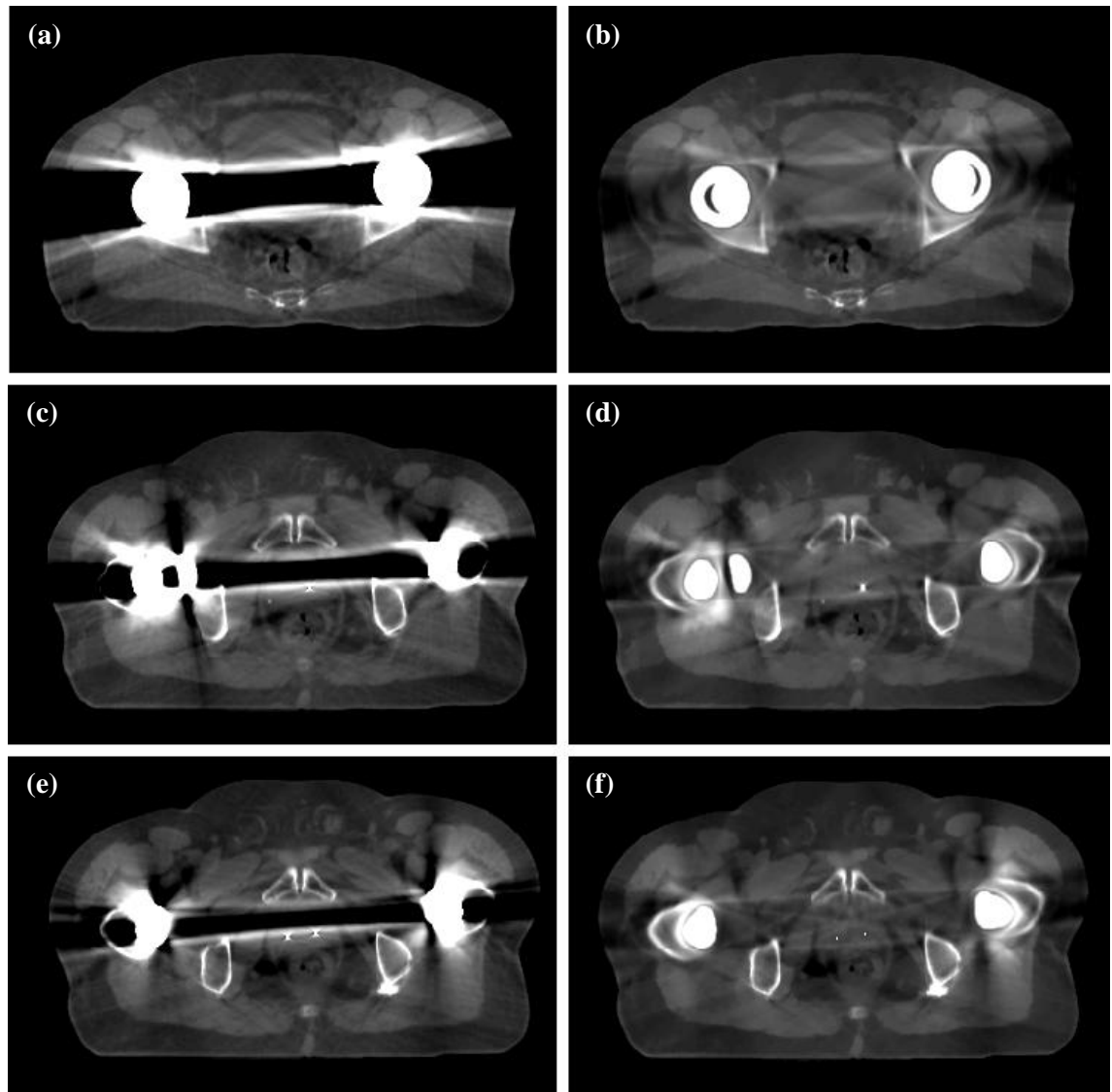


Figure 4.2. CT slice images obtained from the examined double hip prosthesis patient before (left column) and after (right column) CFMAR algorithm application. Top row, middle row and bottom row images depict axial slices of the acetabular cup, transitional and stem section of the metallic hip implants. Note from the middle row images that transition occurs only in the right implant while the left one has already undergone the transition from cup to stem.

From Figure 4.2 one observes an almost total elimination of dark and bright streaks. However, an inclusion of thin bright streaks from the interpolation channel of the algorithm can also be visible. Edge effects in the neighbourhood of metals are reduced with some being still prominent in Figure 4.2f. Although the initial CT images examined in

Figure 4.2 are characterized by lower noise levels compared to the ones in Figure 4.1, a decrease in noise is still present. Similarly to the one hip prosthesis case, metallic parts become more distinguishable from the rest of the image after applying CFMAR. Finally, it is worth noting that despite the incomplete restoration of fat tissue regions and perturbations observed in soft tissue structure contours, the damaged bone contours are recovered and soft tissue structures not visible in the uncorrected images can now be seen.

To provide an overview of the implemented MAR algorithm performance on the whole pelvic CT dataset, coronal slice images for each implant case before and after processing are also provided (Figures 4.3-4.4).

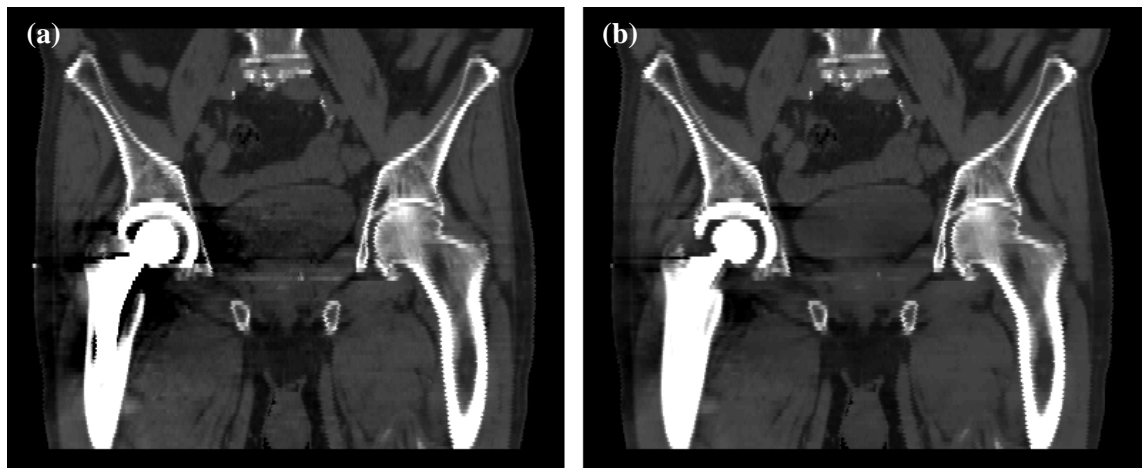


Figure 4.3. Coronal view CT image from the one hip prosthesis patient before (a) and after (b) processing with CFMAR.

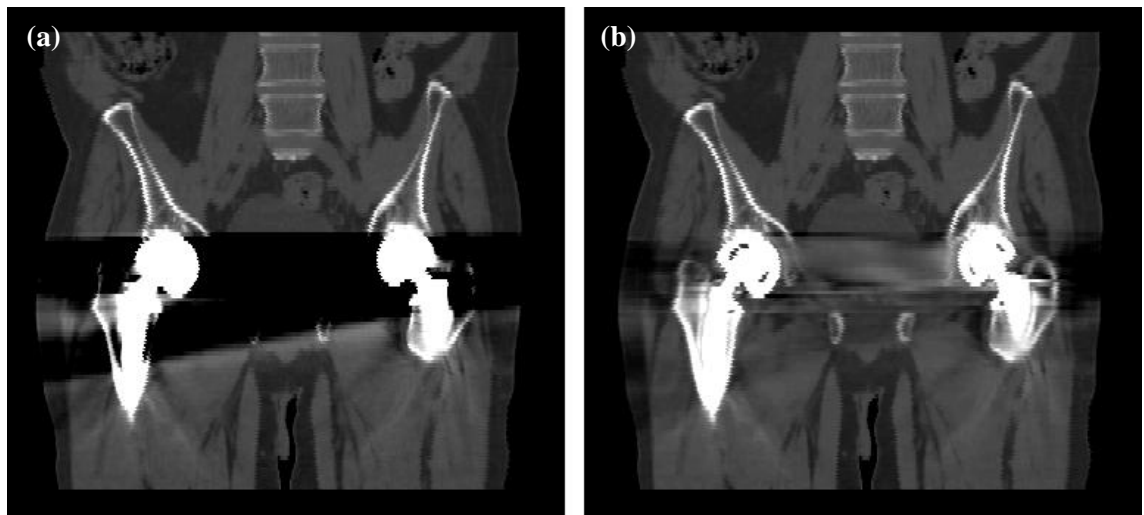


Figure 4.4. Coronal view CT image from the two hip prostheses patient before (a) and after (b) processing with CFMAR.

From the images in Figures 4.3-4.4 the overall MAR properties of the designed algorithm become apparent once again. CFMAR provides structure contour restoration (bladder in Figure 4.3 and bone and body contours in Figure 4.4), noise reduction (blad-

der region from Figure 4.3) and recovery of HU values corrupted by streaking (especially visible from Figure 4.4).

Before proceeding to the next three chapters (Chapters 4.1.1-4.1.3), the axial slice images subjected to sub-image decomposition for a more detailed qualitative analysis of the method are presented with the markings of the respective sub-image locations (Figures 4.5-4.6).

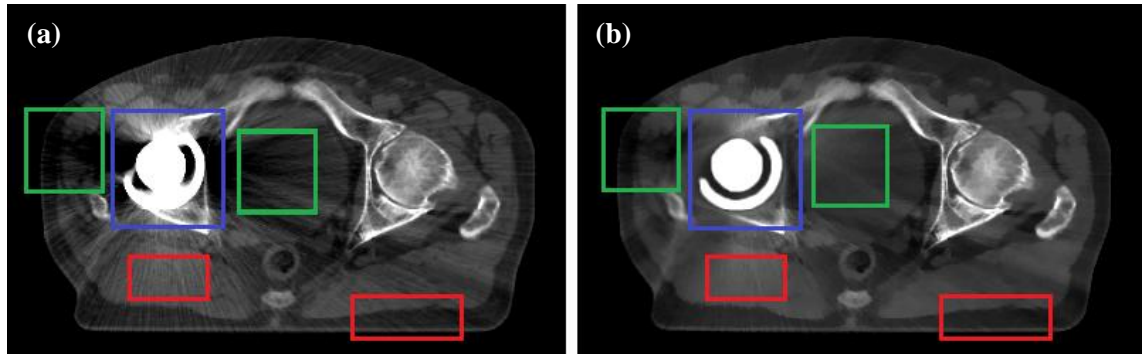


Figure 4.5. Uncorrected (a) and corrected (b) axial CT slice images from the single hip implant pelvic scan with the outlined sub-image locations. The red, green and blue colours correspond to image sections used in further evaluation of de-noising, streak reduction and segmentation components of the algorithm, respectively.

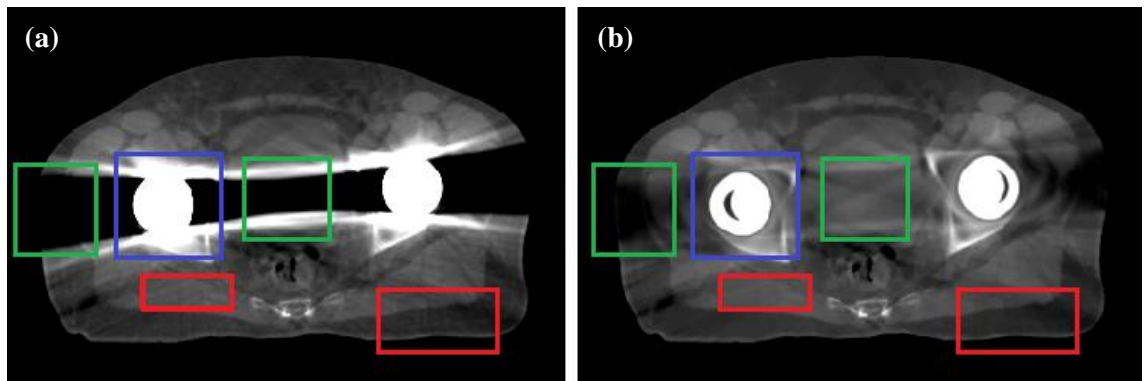


Figure 4.6. Uncorrected (a) and corrected (b) axial CT slice images from the double hip implant pelvic scan with the outlined sub-image locations. The red, green and blue colours correspond to image sections used in further evaluation of de-noising, streak reduction and segmentation components of the algorithm, respectively.

Chapters 4.1.1-4.1.3 will examine the sub-images supplied in Figures 4.5-4.6. Regions outlined with red, blue and green colours will be assessed in Chapter 4.1.1, Chapter 4.1.2 and Chapter 4.1.3, respectively.

4.1.1. De-noising

In this chapter, image sections concerning de-noising efficiency of the introduced MAR method on both hip prostheses cases are examined (Figures 4.7-4.8).

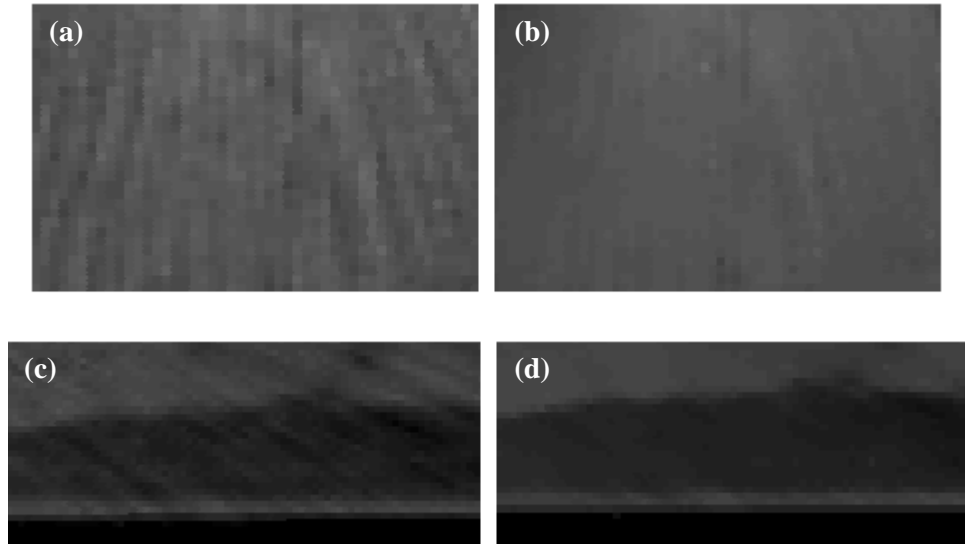


Figure 4.7. Sub-images taken from the CT dataset with a single hip prosthesis to characterize the noise reduction capabilities of the CFMAR algorithm. Left and right columns represent the image regions before and after processing, respectively.

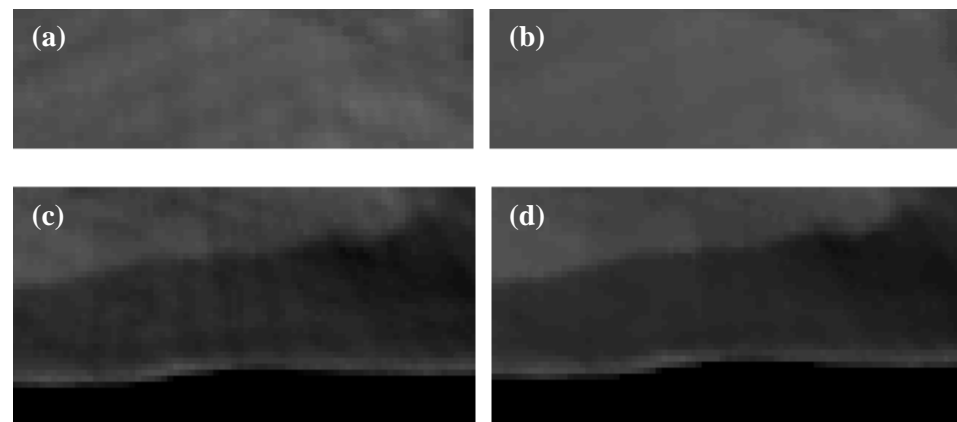


Figure 4.8. Sub-images taken from the CT dataset with double hip prostheses to characterize the noise reduction capabilities of the CFMAR algorithm. Left and right columns represent the image regions before and after processing, respectively.

The observation of Figures 4.7-4.8 indicates the following: the noise reduction filter component of the algorithm preserves edges (bottom row in both figures) and substantially lowers the noise levels (especially visible from Figure 4.7a and Figure 4.7b). The staircase effect of the unmodified BF, discussed in Chapter 3.2.3, is also avoided. Edges are not over-sharpened and no prominent new contours are introduced.

4.1.2. Metal Segmentation

Sub-image regions assessing the performance of the CFMAR algorithm in terms of metal segmentation in both hip implant cases are presented below (Figures 4.9-4.10). Metal objects in both figures belong to the acetabular cup section of the prosthesis.

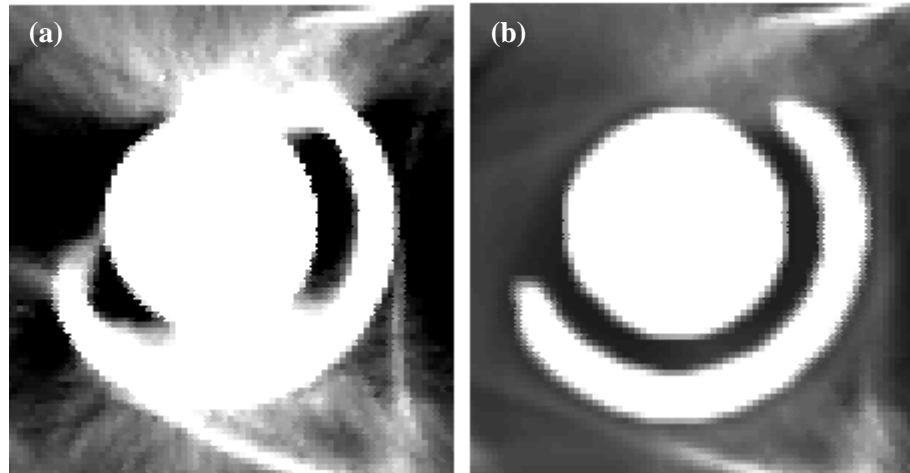


Figure 4.9. Image sections characterizing the metal from the single hip prosthesis case before (a) and after (b) subsection to CFMAR.

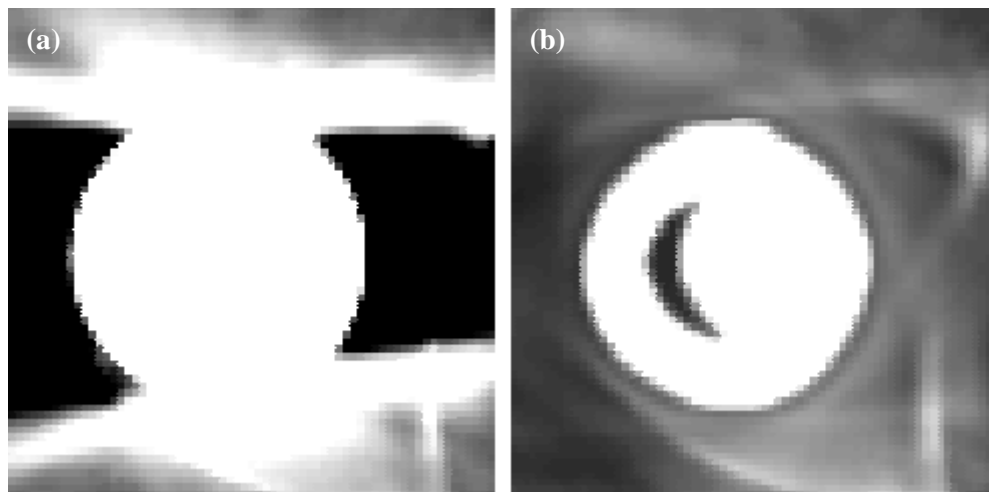


Figure 4.10. Image sections characterizing the metal from the double hip prosthesis case before (a) and after (b) subsection to CFMAR.

Analysis of Figures 4.9-4.10 reflects a successful separation of the metallic parts from the edge effects introduced by them. Individual metal structures are more discernible with the spacing between the head and the outer shell becoming visible (Figure 4.9). Note that the implant design in the one hip prosthesis case differs from the one in the two hip prostheses case (spacing between the shell and the head differs). Lastly, it is worth mentioning that the implant outer shell in Figure 4.9b seems slightly thicker after MAR application.

Finally, the surface reconstructions of the metal objects in both studied pelvic CT scans are presented in Figures 4.11-4.12.

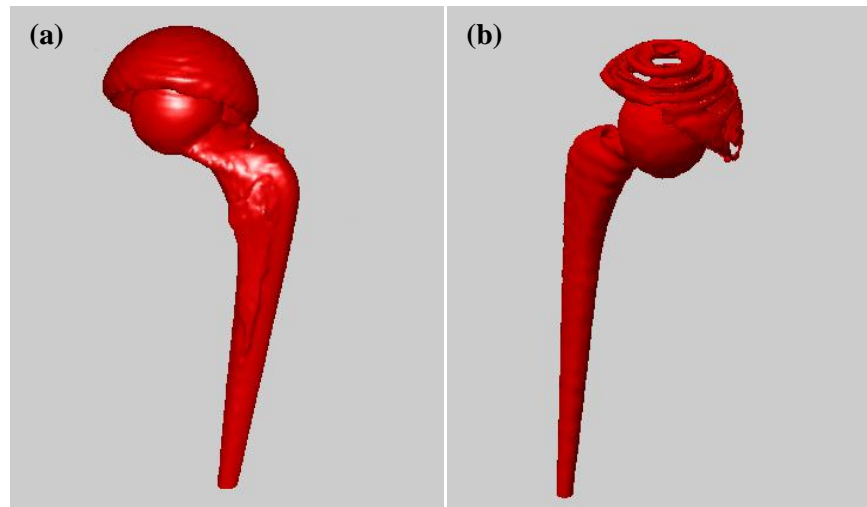


Figure 4.11. 3D surface rendering of metallic structures from the single hip prosthesis case before (a) and after (b) segmentation.

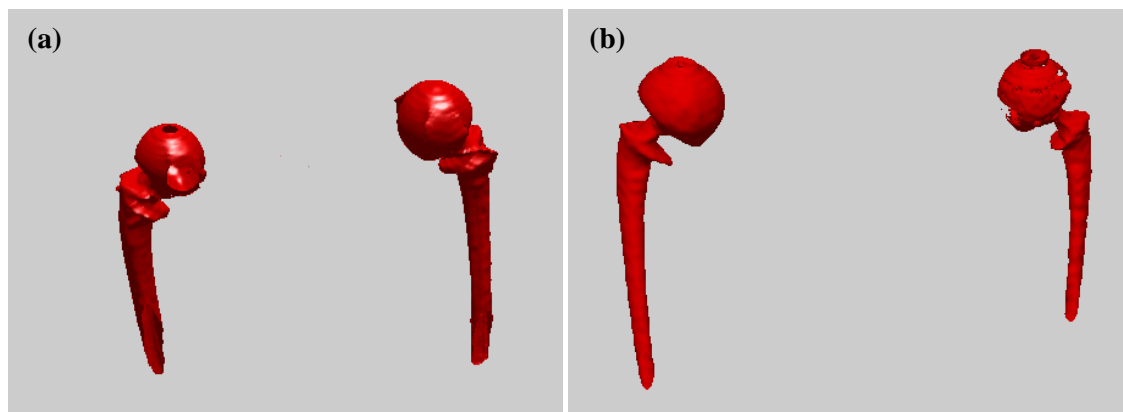


Figure 4.12. 3D surface rendering of metallic structures from the double hip prosthesis case before (a) and after (b) segmentation.

Figures 4.11-4.12 show the exclusion of some parts of the outer shell of the acetabular cup after the segmentation part of the algorithm has been performed. However, the extracted metallic objects depict a successful separation from the edge effects visible in various parts of the objects and a closer resemblance to the real metal hip implants depicted in Figure 2.12 (Chapter 2.2.1).

4.1.3. Reduction of streaking

To finish the qualitative assessment of CFMAR application on the given datasets, one turns to the image regions characterizing streaking. Figure 4.13 presents two sub-images assessing streak artifact correction for the CT dataset containing one hip implant.

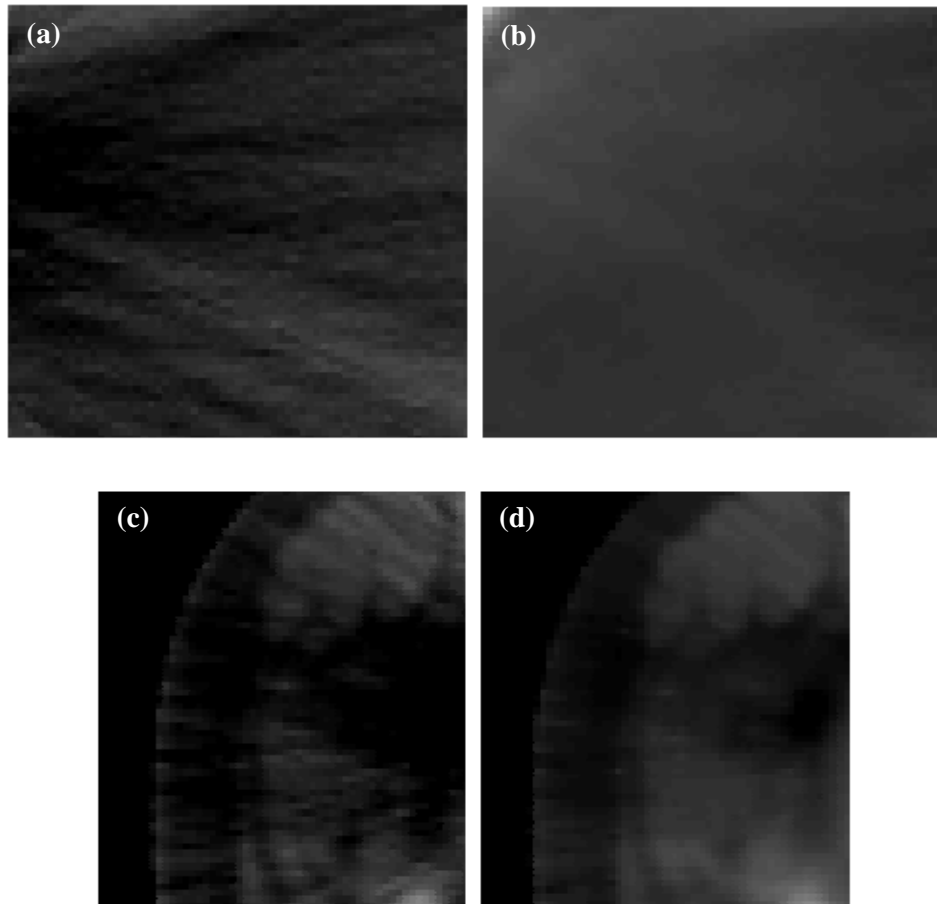


Figure 4.13. Image regions reflecting the streak artifact reduction performance of the designed MAR method in the single hip implant case. Left and right columns display the sections before and after correction. Top and bottom rows depict the bladder and the side sections of the CT image, respectively.

Observation of Figure 4.13 indicates a high degree of streak reduction, with muscle structures becoming more discernible (bottom row) and the distortions in image topology caused by the artifact substantially reduced in their amount. It should be also noted that some artificial contours are introduced after the MAR operation (top row).

A similar figure addressing the streak artifact correction capabilities of the CFMAR in the case of a two hip prostheses containing CT scan is presented below (Figure 4.12).

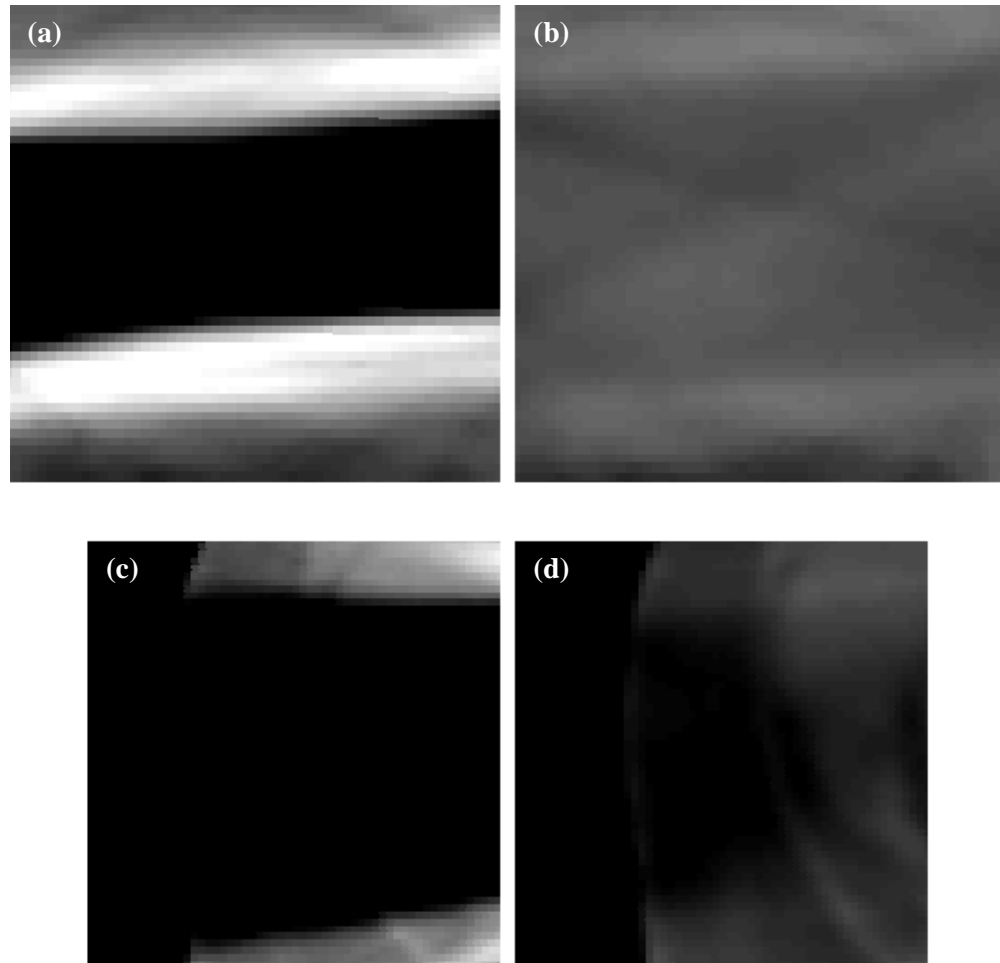


Figure 4.14. Image regions reflecting the streak artifact reduction performance of the designed MAR method in the double hip implant case. Left and right columns display the sections before and after correction. Top and bottom rows depict the bladder and the side sections of the CT image, respectively.

From the left column in Figure 4.11, one observes the effect of streak component of the metal artifact: large regions of lowered HU values (dark zones) and additional regions with CT numbers above their normal value. The application of the CFMAR provides a highly pronounced restoration of these values in both cases. However, it should be pointed out that the fat tissue section is not fully recovered (bottom row) and minor artifacts from the interpolation channel are included in the form blurred dark lines (top row).

4.2. Quantitative Evaluation

A different perspective on the efficiency of the designed MAR algorithm is provided with the aid of ROI measurements and run-time assessment.

The estimated computational time for the two examined pelvic CT scans was: 238.8 ± 2.2 s – one hip implant case and 267.94 ± 0.88 s – two hip implants case. Thus, the algorithm performed faster in the double hip prosthesis case.

The following two chapters (Chapters 4.2.1-4.2.2) present the HU value measurements within the regions specified in Chapter 3.3 in 15 CT slices from both datasets.

4.2.1. The single implant case

Soft tissue ROI measurements performed on 15 representative CT slices from the single hip implant pelvic scan are provided below (Table 4.1).

Table 4.1 HU value measurements in soft tissue regions using fixed size ROIs for the single implant case. Theoretical soft tissue HU value range, as specified by Table 2.1 (Chapter 2.1.4), is +10 to +50 HU.

| Slice number | ROI size, px | ROI mean, HU | |
|--------------|--------------|-------------------|-----------------|
| | | Uncorrected image | Corrected image |
| 1 | 30x30 | -169 ± 69 | -50 ± 12 |
| 2 | 30x30 | -191 ± 67 | -45 ± 15 |
| 3 | 30x30 | -203 ± 73 | -43 ± 20 |
| 4 | 30x30 | -211 ± 77 | -37 ± 21 |
| 5 | 30x30 | -182 ± 66 | -27 ± 16 |
| 6 | 30x30 | -173 ± 74 | -29 ± 16 |
| 7 | 30x30 | -141 ± 67 | -17 ± 15 |
| 8 | 30x30 | -119 ± 66 | -55 ± 24 |
| 9 | 30x30 | -88 ± 68 | -61 ± 48 |
| 10 | 30x30 | -42 ± 62 | -40 ± 31 |
| 11 | 25x25 | -171 ± 74 | -77 ± 29 |
| 12 | 25x25 | -145 ± 63 | -53 ± 23 |
| 13 | 25x25 | -115 ± 61 | -43 ± 22 |
| 14 | 25x25 | -127 ± 56 | -49 ± 38 |
| 15 | 25x25 | -111 ± 62 | -55 ± 49 |

From Table 4.1 the increase in mean HU value within the selected soft tissue regions is apparent. The values in the corrected image are much closer to the approximate theoretical soft tissue norm. Finally, after CFMAR algorithm application, the standard deviations within the corresponding ROIs are decreased up to 5 times (Slice #1).

An equivalent assessment of CT number statistics in fat tissue for the respective metal prosthesis case is given in Table 4.2.

Table 4.2 HU value measurements in fat tissue regions using a fixed size ROI for the single implant case. Theoretical fat tissue HU value range, as specified by Table 2.1 (Chapter 2.1.4), is -100 to -50 HU.

| Slice number | ROI size, px | ROI mean, HU | |
|--------------|--------------|-------------------|-----------------|
| | | Uncorrected image | Corrected image |
| 1 | 10x30 | -213 ± 33 | -174 ± 16 |
| 2 | 10x30 | -216 ± 42 | -171 ± 15 |
| 3 | 10x30 | -219 ± 38 | -171 ± 28 |
| 4 | 10x30 | -213 ± 37 | -178 ± 28 |
| 5 | 10x30 | -203 ± 32 | -179 ± 26 |
| 6 | 10x30 | -217 ± 34 | -175 ± 19 |
| 7 | 10x30 | -243 ± 42 | -188 ± 18 |
| 8 | 10x30 | -260 ± 39 | -221 ± 17 |
| 9 | 10x30 | -261 ± 91 | -190 ± 19 |
| 10 | 10x30 | -225 ± 60 | -203 ± 42 |
| 11 | 10x30 | -213 ± 70 | -210 ± 40 |
| 12 | 10x30 | -197 ± 75 | -196 ± 47 |
| 13 | 10x30 | -191 ± 73 | -181 ± 46 |
| 14 | 10x30 | -194 ± 71 | -178 ± 45 |
| 15 | 10x30 | -201 ± 72 | -177 ± 49 |

Table 4.2 reflects a similar increase in mean CT number values for fat tissue regions. The change is, however, not as prominent as in Table 4.1 with the values still being lower than those specified for fat tissue in Table 2.1. Comparing the standard deviations before and after MAR, one observes a reduction of up to 80% (Slice #9).

4.2.2. The double implant case

An analogous analysis of HU statistics in soft and fat tissue ROIs for the double hip prosthesis case is provided in this chapter. The respective results for soft tissue are given in Table 4.3.

Table 4.3 HU value measurements in soft tissue regions using fixed sized ROIs for the double implant case. Theoretical soft tissue HU value range, as specified by Table 2.1 (Chapter 2.1.4), is +10 to +50 HU.

| Slice number | ROI size, px | ROI mean, HU | |
|--------------|--------------|---|-----------------|
| | | Uncorrected image | Corrected image |
| 1 | 30x30 | $-7.2 \times 10^2 \pm 4.3 \times 10^2$ | 127 ± 32 |
| 2 | 30x30 | $-6.8 \times 10^2 \pm 4.8 \times 10^2$ | 141 ± 39 |
| 3 | 30x30 | $-5.6 \times 10^2 \pm 6.1 \times 10^2$ | 176 ± 45 |
| 4 | 30x30 | $-5.1 \times 10^2 \pm 6.1 \times 10^2$ | 177 ± 45 |
| 5 | 30x30 | $-4.5 \times 10^2 \pm 6.2 \times 10^2$ | 173 ± 43 |
| 6 | 30x30 | $-3.7 \times 10^2 \pm 7.3 \times 10^2$ | 156 ± 55 |
| 7 | 30x30 | $-3.5 \times 10^2 \pm 7.3 \times 10^2$ | 98 ± 92 |
| 8 | 25x25 | $-3.9 \times 10^2 \pm 6.6 \times 10^2$ | 112 ± 69 |
| 9 | 25x25 | $-2.5 \times 10^2 \pm 6.5 \times 10^2$ | 172 ± 32 |
| 10 | 25x25 | $-1.5 \times 10^2 \pm 5.4 \times 10^2$ | 106 ± 27 |
| 11 | 25x25 | $-1.5 \times 10^2 \pm 5.0 \times 10^2$ | 125 ± 41 |
| 12 | 25x25 | $-1.3 \times 10^2 \pm 4.6 \times 10^2$ | 101 ± 43 |
| 13 | 25x25 | $-1.1 \times 10^2 \pm 4.2 \times 10^2$ | 108 ± 41 |
| 14 | 25x25 | $-0.89 \times 10^2 \pm 3.7 \times 10^2$ | 87 ± 48 |
| 15 | 25x25 | $-0.77 \times 10^2 \pm 3.5 \times 10^2$ | 76 ± 47 |

In comparison with Table 4.1, the mean HU values show a substantial improvement from the highly lowered values in the uncorrected images. Note also the high standard deviations compared to Table 4.1. Once again, the CT numbers obtained after processing with CFMAR are closer to theoretical ones. Finally, after image correction, a much lower standard deviation in the homogeneous soft tissue regions is exhibited: up to 95% decreased (Slice #9). The change is even more pronounced, if compared to Table 4.1.

A similar overview of HU value statistics in fat tissue for the corresponding metal hip implant case is given in Table 4.4.

Table 4.4 HU value measurements in fat tissue regions using a fixed size ROI for the double implant case. Theoretical fat tissue HU value range, as specified by Table 2.1 (Chapter 2.1.4), is -100 to -50 HU.

| Slice number | ROI size, px | ROI mean, HU | |
|--------------|--------------|--|-----------------|
| | | Uncorrected image | Corrected image |
| 1 | 10x30 | -501 ± 37 | -233 ± 27 |
| 2 | 10x30 | -454 ± 48 | -219 ± 22 |
| 3 | 10x30 | -422 ± 39 | -198 ± 27 |
| 4 | 10x30 | -386 ± 54 | -183 ± 28 |
| 5 | 10x30 | -350 ± 33 | -157 ± 28 |
| 6 | 10x30 | -332 ± 37 | -161 ± 30 |
| 7 | 10x30 | -437 ± 52 | -150 ± 28 |
| 8 | 10x30 | $-5.8 \times 10^2 \pm 1.2 \times 10^2$ | -145 ± 40 |
| 9 | 10x30 | $-5.0 \times 10^2 \pm 1.6 \times 10^2$ | -102 ± 63 |
| 10 | 10x30 | $-3.5 \times 10^2 \pm 1.2 \times 10^2$ | -131 ± 54 |
| 11 | 10x30 | $-3.3 \times 10^2 \pm 1.6 \times 10^2$ | -69 ± 46 |
| 12 | 10x30 | $-3.2 \times 10^2 \pm 2.1 \times 10^2$ | -52 ± 69 |
| 13 | 10x30 | $-2.8 \times 10^2 \pm 2.3 \times 10^2$ | -35 ± 73 |
| 14 | 10x30 | $-2.4 \times 10^2 \pm 2.2 \times 10^2$ | -55 ± 71 |
| 15 | 10x30 | $-2.2 \times 10^2 \pm 2.2 \times 10^2$ | -53 ± 67 |

Table 4.4 presents lower fat tissue values before MAR than the ones provided in Table 4.2. After correction the mean HU values and the standard deviations are increased and reduced, respectively. Some mean CT numbers also fall into the normal fat tissue range (Slices #11-15). The standard deviation has been reduced approximately up to 3 times (Slice #8 and Slices #12-15).

5. DISCUSSION

With the results of applying the designed metal artifact correction technique presented in Chapter 4, it now becomes feasible to give a thorough assessment of the method. This is done by analyzing the CFMAR algorithm performance in terms of various aspects like CT image de-noising (Chapter 5.1), metal segmentation (Chapter 5.2), reduction of streaking (Chapter 5.3) and computational speed (Chapter 5.4).

Potential improvements to the designed MAR method are mentioned throughout Chapters 5.1-5.4. Future plans concerning further method development are also discussed (Chapter 5.5).

5.1. De-noising performance

Noise was considered one of the major components of the overall metal artifact, as outlined in Chapter 2.2. The filter channel of the CFMAR (Figure 3.3) was responsible for lowering the levels of noise introduced by the metal artifact. Filtering was based on applying the GBF introduced in Chapter 3.2.3.

Results showed a significant amount of noise reduction in pelvic CT datasets containing both one and two metal hip implants (Chapter 4.1 and Chapter 4.1.1). This has been confirmed through the qualitative assessment of images in Figures 4.1-4.4 and Figures 4.7-4.8.

Although the classical BF had the properties of edge preservation and noise reduction as outlined in Chapter 3.2.3, it was also prone to introduction of staircase effects in the image and edge over-sharpening [32; 34]. Qualitative analysis indicated the GBF part of the designed MAR technique not only to reduce image noise (especially visible in Figure 4.7), but also to preserve edges and avoid the introduction of new contours (Figures 4.7-4.8). Thus, the drawbacks of the BF have been eluded. It is also worth mentioning that since noise causes the HU values to deviate from normal, the filtering operation also contributes (to some degree) to the overall CT number accuracy in the examined datasets. This acts as an improvement in radiotherapy dose calculations, as outlined in Chapter 2.2.2. Additionally, structure delineation becomes less cumbersome in the noise reduced images with better contour visibility.

However, by examining the axial CT images from Figures 4.1-4.2, one can witness the loss of certain fine anatomical detail in the process of filtering. This is immediately visible in Figure 4.1, when examining muscle tissue regions. This undesirable effect cannot be completely avoided due to the fact that the designed filter is still a low-pass filter, although non-linear. The edge preservation property outlined by (3.4) is based on the range Gaussian component which relates to the pixel intensity differences. The

range spread parameter σ_r controls which pixels are included in the averaging. Loosely speaking, it defines the “minimum” edge amplitude to be preserved. Given that fine anatomical detail exhibits a local intensity difference in the same (or even a smaller scale) than image noise, it will also be averaged out (smoothed). Hence, one can adjust the range parameter, but there will always be a compromise between fine edge conservation and noise reduction. Another issue to be considered is that the interpretation of images is a subjective matter [33]. Thus, whether some perturbations in the CT image HU values are noise or anatomical detail, may very well be an open question.

It should be noted that the filtering technique implemented in this thesis might not provide the best possible de-noising performance. Possible modifications of the filter channel may include the use of a more advanced method such as those based on non-local filtering [35; 36; 37], PDEs [38; 39] or wavelets [40].

One typical example of non-local filtering is the non-local means (NLM) algorithm introduced by Buades et al. [35]. It is based on computing the weighted similarities between pixel neighbourhoods followed by averaging. The averaging is weighted according to the level of similarity. This approach provides noise reduction properties superior to that of the BF and has been successfully implemented in de-noising of abdominal CT images [36]. Since the modification administered to the BF in this work was not aimed to improve the noise removing performance, the NLM algorithm would be expected to produce better results in terms of noise. However, due to the non-local nature of this technique, the computational time can be much greater than that of the GBF. Still, the computation of similarities for the NLM method can be accelerated [37].

PDE methods for image de-noising are a quite promising approach with a vast selection of models suitable for a given application [38]. Modern non-linear PDE methods, such as the structure tensor based non-linear diffusion, can provide better performance than the GBF [39]. However, similar to the PDE techniques used for sinogram interpolation (Chapter 2.3), they involve a significant amount of iterations to acquire the desired result. Thus, using such methods for the filtering part of the CFMAR will make the algorithm run slower.

Another alternative for the filter channel is wavelet based noise reduction [40]. The general idea is to separate the image in terms of frequency components and remove those carrying noise. Although, being faster than both PDE and NLM methods and providing promising results in terms of additive Gaussian noise removal, it remains to be seen how this particular technique performs in comparison with the filtering method implemented in this thesis.

5.2. Segmentation of metallic parts

Identification of metallic regions was not only crucial in providing the ability to change the inaccurate HU values within the metal structures (Chapter 3.2.4), but also in identifying the sinogram area where LI should be performed (Chapter 3.2.5). An intelligent

thresholding approach utilizing pixel connectivity was implemented to address this segmentation problem (Chapter 3.2.4).

Results provided a qualitative analysis of segmentation performance on both CT slice images and a 3D surface model of the respective metallic structures before and after processing with CFMAR (Chapter 4.1 and Chapter 4.1.2). From the images provided in Figures 4.1-4.2 and Figures 4.9-4.10, one observes the separation of these structures from the EEGE effect produced by them. Contours become more discernible from the rest of the image and the spacing between the outer shell and the femoral head of the implant is now more apparent. This spacing is expected because the attenuation of polyethylene is significantly lower than that of the metals used in hip implants. There is also a slight thickening of the outer shell cross-section area observed in Figure 4.9 as a result of Gaussian filtering applied on the metal mask and display window parameters. Because of the mapping of HU values to the 8-bit scale of the monitor described in Chapter 2.1.4, adjacent values are viewed as a single value on the monitor. After filtering the resulting metal structure edges are blurred and the region occupied by the structure becomes larger. Although the new values introduced around the metal are lower in intensity, they are still close enough for the visualization mapping to convert them to a single value.

The 3D view of the metallic structures (Figure 4.11-4.12), shows a similar pattern in terms of metal extraction from the edge effects and separation of individual implant objects. However, the surface renderings also show that some parts of outer shell are lost as a result of segmentation. This is an unfortunate result of the slice based thresholding and connectivity operations. Nevertheless, the 3D models after processing show a better correspondence to the example implant models presented in Chapter 2.2.1 (Figure 2.12) with a more even stem structure, better outer shell and femoral head separation and the exclusion of additional structures around the upper part of the stem.

As with noise reduction (Chapter 5.1), the enhanced visibility of metal implant structure contours provides better performance in the delineation process during radiotherapy treatment planning with respect to these structures. Furthermore, the ability to replace the high CT number values in the metallic structures with a user specified value acts as an improvement in dose calculations, if the patient's implant composition is known or can be determined from an experimentally obtained correspondence between saturated HU values and the respective metal type these values represent.

It must be noted that the intensity based segmentation approach was chosen due to the broad CT number scale of the used scanner which makes it simpler to separate objects in terms of intensity. The method is not optimal for the restricted scale of 4096 gray levels and must still be refined in terms of the threshold levels. A modification to volume intelligent thresholding and voxel connectivity can possibly provide better results for both types of CT number ranges. Segmentation model robustness to different gray level scales and improvement in performance can be achieved with the aid of several alternative methods like mutual information based segmentation [24], region growing and morphology [41] and level sets [42].

Extraction of metal regions through the use of mutual information has already been seen as part of a MAR method [24]. The idea is to decompose the image into smaller sub-images based on local intensity statistics and then group the images together in such a way that the mutual information (characterized by joint entropy) is maximized. The method proved to be promising with respect to metallic clips and dental fillings, but it remains to be seen how it relates to pelvic hip implants. [24]

Region growing is a classical segmentation method based on the principle of adding pixels (or voxels) to seed points located in the object to be extracted. The addition is performed utilizing a certain similarity metric (intensity, gradient, et cetera) [33]. The use of morphological image operations in combination with the distance transform in the work by Yussuf et al. [41] help define the initial seeds. Afterwards, the region growing process is initiated and intensity statistics based operations help refine the result. Although implemented for liver segmentation, the method has potential for solving the current problem with proper modifications: better seed selection procedure, use of geometrical information about the metal implant to improve the performance of region growing. [41]

3D segmentation of bone structures has successfully been achieved through the use of a fast level set method described by Krátký et al. [42]. The method is based on object contour evolution through functional minimization. The process involves iterations with a stopping criterion specified by the user. Despite the iterative nature of the method, it is still computationally fast. Although promising results on bone extraction have been exhibited, the performance of the discussed level set technique on metallic structures remains a matter of further assessment. [42]

Lastly, an alternative approach in metal object segmentation from metal artifact corrupted CT images should be mentioned. Instead of segmenting the metal object in the image domain, the operation is performed directly in the projection domain by using a Markov random field model. Such an approach can provide a better estimate of the sinogram traces used in LI as well as a good separation of metal objects in the image domain after reconstruction. [43]

5.3. Reduction of streaking

From Chapter 2.2.1 (Figures 2.14-2.15) one observes how the streak component of the metal artifact causes the most significant inaccuracies in HU values of CT images and perturbs the consistency of anatomical contours. Interpolation of metal affected projection domain regions (Chapter 3.2.5) along with CFMAR channel weighting scheme (Chapter 3.2.6) aimed to correct for these effects without introducing new artifacts in the resulting image.

Through the visual assessment of Figures 4.1-4.4 and Figures 4.13-4.14 (Chapter 4.1 and Chapter 4.1.3) and considering the homogeneous ROI measurements provided in Tables 4.1-4.4 (Chapter 4.2), the substantial reduction of streaking is apparent.

Figures 4.1-4.4 and Figures 4.13-4.14 show an overall improvement in tissue HU values and anatomical contour consistency in regions corrupted by the metal artifact after applying CFMAR. In terms of structure contours this is especially prominent when observing the bladder in Figure 4.1 (top row) and Figure 4.3, and the bone structures in Figure 4.2 and Figure 4.4. However, the restoration is incomplete with HU values still being lowered in the fat tissue regions in the implant vicinity in both studied cases. The same can be observed for some soft tissue regions in the one implant case (top row of Figure 4.1). Additionally, in the two implant case, bladder contours are blurred out and new artifacts are introduced in the form of thin lines aligned in the direction of the dark and bright streaks observed in the uncorrected images of Figure 4.2 and Figure 4.4. Other line-like distortions are also visible within the restored region between the metallic objects in the images corresponding to the double hip prosthesis case (top row of both Figure 4.2 and Figure 4.14). Finally, from the examination of Figures 4.13-4.14, one notes the presence of false contours.

The numerical data from Tables 4.1-4.4 acts in support of the previous observations made from the qualitative evaluation of CFMAR. In both implant cases soft and fat tissues exhibit an improvement in terms of the lowered initial HU mean values and high standard deviations. The improvement is most pronounced in the double metallic hip implant case (Tables 4.3-4.4). Results also depict the assessed tissue regions becoming more homogeneous with the standard deviations being decreased up to 95% in some images (Slice #9, Table 4.3). Additionally, the mean values after processing with the designed MAR method become closer to the approximate soft and fat tissue HU value ranges provided in Table 2.1 (Chapter 2.1.4): values for soft tissues are lower and higher than normal in the single and double implant cases, respectively, and values for fat tissue are mostly lower than normal in both cases (except Slices #11-15, Table 4.4). Lower than normal HU values of soft tissues in the single implant case were already detected from the analysis of Figure 4.1 and Figure 4.3. The increased soft tissue HU values indicated by Table 4.3 in the double implant case are a result of the ROI incorporating the thin bright line artifacts observed in Figure 4.2, thus, contributing to the increased mean value.

The incomplete or inaccurate recovery of metal artifact corrupted regions discussed above is a product of several factors affecting the interpolation channel, which is used as the primary source of information for restoring distorted image areas. Firstly, due to the unavailability of raw projection data, it is approximated via parallel beam RT from the initial CT images. As a result, the ray sums of the rays passing through image regions where metal artifact is present do not produce accurate projection values. Additionally, the sinogram interpolation method (LI) used in the study may not provide the best recovery for the regions containing metal. Finally, the identification of metal traces through RT projection of segmented metal object in the approximated projection domain can also introduce some degree of inaccuracy. Furthermore, even with adjustments, the weight mask may not completely mimic the artifact distribution, since the

reconstruction algorithm used in this work (FBP) is different from the one implemented in the CT machine (FDK).

The false contour effect visible in Figures 4.13-4.14 is, once again, the result of window display of the examined CT images. With the replacement of multiple adjacent gray levels with a single one, smooth image regions having fine gray values may exhibit sharper transitions as a result.

It must also be noted that HU is a energy dependent parameter and this dependence is not identical among different anatomical tissues. Furthermore, the CT number scale may not be the same for various CT scanner vendors. [44] This can give another source for the mean HU value deviation (Tables 4.1-4.4) from the theoretical norm for respective tissues (Table 2.1).

Despite the discussed CT number inaccuracies and inclusion of some additional artifacts, the streaking correction incorporated in the CFMAR produces images with a much more informative view of the patient's anatomy with HU values being far more coherent with the correct ones for the respective tissues. The major role of the streak metal artifact component in the overall image corruption entails a significant contribution to structure delineation and dose calculation accuracy in radiotherapy treatment planning.

A superior streaking reduction could be achieved, if raw projection data was available. Additionally, by applying the same projection acquisition geometry with the corresponding reconstruction algorithm as in the CT scanner used in image generation, a better artifact distribution weight mask can be composed. However, the acquisition geometry and reconstruction algorithm can vary between different CT machine vendors. Furthermore, they can be far more complex and difficult in implementation. The FDK algorithm used in the CT scanner considered in this study, for example, is intended for cone-beam geometry which deals with multislice image acquisition and reconstruction with rays traversing the patient at certain angles [45]. One must also note that the manufacturer may not provide an exact (if any) specification of the reconstruction algorithm implemented in the CT machine.

Another improvement to the streak component correction of the metal artifact can be obtained through modifications to the interpolation channel of the CFMAR algorithm. Improved segmentation of metal regions either in the image or sinogram domains and a more complex interpolation technique can contribute to a more accurate interpolation result. The possible replacements for LI can include interpolation based on coherence transport [27], pixel neighbourhood statistics [46], wavelets [47], PDEs [48] and sinusoidal structure of the sinogram [49]. For possible alternative methods to augment metal segmentation performance, the reader is referred to Chapter 5.2.

As already noted in Chapter 2.3, coherence transport sinogram inpainting shows interpolation results superior to LI in the case of numerical phantom images simulating metal artifacts [27]. Further investigation of the work by Bornemann et al. [50], which served as the basis for this MAR method, indicated a high mathematical complexity of the algorithm implementation as well as a large number of free parameters. The speed

of the algorithm, however, enables the fast adjustment of these parameters. Thus, the only drawbacks of this approach are implementation complexity and the absence of evaluation on clinical data (Chapter 2.3).

Non-local methods in the studies of Bornard et al. [46] and Ignácio et al. [47] are both based on a similar approach utilized in the image and wavelet domains, respectively. The idea is to inpaint the considered region inward from the available data by comparing pixel neighbourhoods of pixels to be inpainted and those lying in the correct data image section. There is one difference in the two techniques: Bornard et al. [46] interpolates individual pixels, while Ignácio et al. [47] interpolates entire blocks. Both methods show excellent performance on natural images, but the effect in the sinogram domain remains a matter of assessment.

The PDE interpolation method introduced by Brito-Loeza et al. [48] implements a certain acceleration scheme enabling it to perform much faster than the PDE approaches discussed in Chapter 2.3. However, implementation complexity also increases. Since PDE methods have already shown performance superior to LI, this technique can provide a good alternative to the one implemented in this work.

The best alternative could be, however, the projection domain inpainting approach outlined in the study by Li et al. [49]. The method exploits the sinusoidal structure of the sinogram considering each interpolation point to be located within a group of sinusoid-like curves, thus, providing preservation of texture continuity in the sinogram. The method shows promising results dealing with missing projection data due to sparse sampling and detector gaps.

5.4. Computational speed

Chapter 4.2 showed an example CFMAR performance speed for the studied one and two metallic hip implant cases to be approximately 4.5 and 4 minutes, respectively. Both cases exhibited a similar number of slices: 60 and 65 in the single and double implant CT datasets, respectively. Observed short computational times entail fast adjustments of CFMAR free parameters by the operator.

The computation is slightly faster in the double implant case due to a less complex channel weight mask structure (Chapter 3.2.6). In practice the processing time will be not only be affected by the number of hip implants present in the anatomy, but by the number of slices with metal present in the CT dataset under consideration.

Certain approaches can be applied to further accelerate the designed metal artifact correction algorithm. These include the use of another programming language [51] and parallel computing [52].

The programming language implemented in this study for MAR method design (MATLAB) is an interpreted language. Thus, each time a line of code is encountered, an interpretation of the meaning must be obtained before execution. This entails a slower performance inside any loops. The solution is to perform these calculations using a compiled language program and then let MATLAB call the respective file(s). [51]

A programmable graphics processing unit (GPU) has proven to be a powerful resource for overall computing. Previous research has indicated that using GPUs for local image processing operations entails shorter computational times than in the case of a central processing unit (CPU). GPUs provide the ability to implement a higher degree of parallel computation than CPUs. [53]. MATLAB provides GPU based versions of some of its key functions, which can be easily implemented, if the computer used for algorithm execution has a compatible graphics card.

5.5. Future work

Although the designed algorithm showed significant improvements in resulting clinical CT images in terms of metal artifact reduction, the quantification of the impact on dose calculation accuracy in radiotherapy treatment planning remains a matter of further investigation. For this reason a physical phantom containing a hip implant model will be subjected to CT scanning and then CFMAR application. Afterwards, the respective dose calculations will be performed before and after MAR to assess the changes.

Chapters 5.1-5.4 listed possible improvements to the individual steps of the designed MAR method and overall computational time. Future studies will be considered with testing the alternative methods suitable for CFMAR de-noising, segmentation and streaking reduction components as well as with the method implementation correction in the direction of GPU based parallel computing.

Finally, it is also possible to optimize the channel weight mask construction for metal artifact distributions from other CT scans corrupted by metal artifact. These may include thoracic and head CT scans, for example.

6. CONCLUSION

In this thesis a novel MAR method was designed in order to improve structure delineation and dose calculation accuracy in radiotherapy considering pelvic CT images with metallic hip prostheses. Both qualitative and quantitative performance assessment of the method was carried out. Visual evaluation of the corrected CT images indicated a substantial reduction in terms of all metal artifact components and a more accurate metal object structure representation. Improvements in tissue HU value accuracy and anatomical structure contour consistency were achieved. The superior accuracy of CT numbers in the images corrected by the designed algorithm was additionally confirmed through quantitative measurements.

REFERENCES

- [1] Bushberg, J.T., Siebert, J.A., Leidholdt, E.M.Jr. & Boone, J.M. The essential physics of medical imaging. 2nd edition. Philadelphia 2002, Lippincott Williams & Wilkins. 933 p.
- [2] Dougherty, G. Digital image processing for medical applications. New York 2009, Cambridge University Press. 462 p.
- [3] Jan, J. Medical image processing, reconstruction and restoration: concepts and methods. Boca Raton 2006, CRC Press. 730 p.
- [4] Fessler, J.A. Statistical Methods for Image Reconstruction. Rome 2004, NSS/MIC. Unpublished short course notes. 87 p.
- [5] Podgorsak, E.B. Radiation oncology physics: a handbook for teachers and students. Vienna 2005, International Atomic Energy Agency. 657 p.
- [6] Boas, F.E. & Fleischmann, D. Computed tomography artifacts: Causes and reduction techniques. *Imaging in Medicine*, 4(2012)2, pp. 229-240.
- [7] Task Group 63 of Radiation Therapy Committee of the American Association of Physicists in Medicine (AAPM). Dosimetric considerations for patients with hip prostheses undergoing pelvic irradiation. *Medical Physics*, 30(2003)6, pp. 1162-1182.
- [8] Deasy, J.O., Blanco, A.I. & Clark, V.H. CERR: a computational environment for radiotherapy research. *Medical Physics*, 30(2003)5, pp. 979-985.
- [9] Hsieh, J. Computed Tomography Principles, Design, Artifacts, and Recent Advances. 2nd edition. Washington 2009, Wiley & SPIE Press. 510 p.
- [10] Rao, N.P., Srirangam, S.J. & Preminger, G.M. Urological tests in clinical practice. London 2007, Springer-Verlag. 291 p.
- [11] De Man, B., Nuyts, J., Dupont, P., Marchal, G. & Suetens, P. Metal streak artifacts in x-ray computed tomography: a simulation study. *IEEE Transactions on Nuclear Science*, 46(1999)3, pp. 691-696.
- [12] Boas, F.E. & Fleischmann, D. Iterative techniques for metal artifact reduction. San Francisco 2011, presented at the International Society for Computed Tomography meeting. Unpublished presentation. 36 p.
- [13] Joseph, P.M. & Spital, R.D. The exponential edge-gradient effect in x-ray computed tomography. *Physics in Medicine & Biology*, 26(1981)3, pp. 473-487.
- [14] Saw, C.B., Loper, A., Komanduri, K., Combine, T., Huq, S. & Scicutella C. Determination of CT-to-density conversion relationship for image-based treatment planning systems. *Medical Dosimetry* 30(2005)3, pp. 145-148.

- [15] Li, H., Noel, C., Chen, H., Harold Li, H., Low, D., Moore, K., Klahr, P., Michalski, J., Gay, H. A., Thorstad, W. & Mutic, S. Clinical evaluation of a commercial orthopedic metal artifact reduction tool for CT simulations in radiation therapy. *Medical Physics* 39(2012)12, pp. 7507-7517.
- [16] Finnish Cancer Registry [WWW]. [Accessed on 9.04.2013]. Available at: <http://www.cancer.fi/syoparekisteri/en/>
- [17] Abdoli, M., Dierckx, R.A., Zaidi, H. Metal artifact reduction strategies for improved attenuation correction in hybrid PET/CT imaging. *Medical Physics*, 39(2012)6, pp. 3343-3360.
- [18] Boas, F.E. & Fleischmann, D. Evaluation of two iterative techniques for reducing metal artifacts in computed tomography. *Radiology*, 259 (2011)3, pp. 894-902.
- [19] De Man, B., Nuyts, J., Dupont, P., Marchal, G. & Suetens, P. Reduction of metal streak artifacts in x-ray computed tomography using a transmission maximum a posteriori algorithm. *IEEE Transactions on Nuclear Science*, 47(2000)3, pp. 977-981.
- [20] Zhang, X., Wang, J., Xing, L. Metal artifact reduction in x-ray computed tomography (CT) by constrained optimization. *Medical physics*, 38(2011)2, pp. 701-711.
- [21] Kalender, W., Hebel, R. & Ebersberger, J. Reduction of CT artifacts caused by metallic implants. *Radiology* 164(1987)2, pp. 576-577.
- [22] Zhang, Y., Pu, Y.F., Hu, J.R., Liu, Y., Chen, Q.L. & Zhou, J.L. Efficient CT metal artifact reduction based on fractional-order curvature diffusion. *Computational and Mathematical Methods in Medicine*, 2011(2011), 9 p.
- [23] Yu, H., Zeng, K., Bharkhada, D.K., Wang, G., Madsen, M.T., Saba, O., Policeni, B., Howard, M.A. & Smoker, W.R. A segmentation-based method for metal artifact reduction. *Academic Radiology*, 14(2007)4, pp. 495-504.
- [24] Chen, Y., Li, Y., Guo, H., Hu, Y., Luo, L., Yin, X., Gu, J. & Toumoulin, C. CT metal artifact reduction method based on improved image segmentation and sinogram inpainting. *Mathematical Problems in Engineering*, 2012(2012), 18 p.
- [25] Choi, J., Kim, K.S., Kim, M.W., Seong, W. & Ye, J.C. Sparsity driven metal part reconstruction for artifact removal in dental CT. *Journal of x-ray Science and Technology*, 19(2011)4, pp. 457-475.
- [26] Duan, X., Zhang, L., Xiao, Y., Cheng J., Chen, Z. & Xing, Y. Metal artifact reduction in CT images by sinogram TV inpainting. *Proceedings of the IEEE Nuclear Science Symposium Conference*, Dresden, Germany, 19-25 October, 2008, IEEE, pp. 4175-4177.

- [27] Zhang, Y., Pu, Y.F., Hu, J.R. & Zhou, J.L. Fast x-ray CT metal artifacts reduction based on noniterative sinogram inpainting. Proceedings of the Nuclear Science Symposium and Medical Imaging Conference, Valencia, Spain, 23-29 October, 2011, IEEE, pp. 2462-2464.
- [28] Watzke, O. & Kalender, W.A. A pragmatic approach to metal artifact reduction in CT: merging of metal artifact reduced images. *European Radiology*, 14(2004)5, pp. 849-856.
- [29] Kachelriess, M., Watzke, O. & Kalender, W.A. Generalized multidimensional adaptive filtering for conventional and spiral single-slice, multi-slice, and cone-beam CT. *Medical Physics*, 28(2001)4, pp. 475-490.
- [30] US patent 8233586. Iterative reduction of artifacts in computed tomography images using forward projection and an edge-preserving blur filter. Boas, F.E. Application number 13/030088, 17.02.2011 (31.07.2012). 10 p.
- [31] Tomasi, C. & Manduchi, R. Bilateral filtering for gray and color images. Proceedings of the International Conference on Computer Vision, Bombay, India, 4-7 January, 1998, IEEE, pp. 839-846.
- [32] Paris, S., Kornprobst, P., Tumblin, J. & Durand, F. A gentle introduction to bilateral filtering and its applications [WWW]. [Accessed on 13.04.2013]. Available at: http://people.csail.mit.edu/sparis/bf_course/
- [33] Gonzales, R.C. & Woods, R.E. *Digital Image Processing*. 2nd edition. Upper Saddle River 2002, Prentice Hall, 793 p.
- [34] Buades, A., Coll, B. & Morel, J.M. The staircasing effect in neighborhood filters and its solution. *IEEE Transactions on Image Processing*, 15(2006)6, pp. 1499-1505.
- [35] Buades, A., Coll, B. & Morel, J.M. A non-local algorithm for image denoising. Proceedings of the 2005 IEEE Computer Society Conference on Computer Vision and Pattern Recognition, San Diego, California, USA, 20-25 June, 2005, IEEE, pp. 60-65.
- [36] Chen, Y., Chen, W., Yin, X., Ye, X., Bao, X., Luo, L., Feng, Q., Li, Y. & Yu, X. Improving low-dose abdominal CT images by Weighted Intensity Averaging over Large-scale Neighborhoods. *European Journal of Radiology*, 80(2011)2, pp. e42-e49.
- [37] Liu, Y.L., Wang, J. & Chen, X. A robust and fast non-local means algorithm for image denoising. *Journal of Computer Science and Technology*, 23(2008)2, pp. 270-279.
- [38] Weickert, J. *Anisotropic Diffusion in Image Processing*. Stuttgart 1998, Teubner, 184 pp.

- [39] Benzarti, F. & Amiri, H. Image denoising using non linear diffusion tensors. *Advances in Computing*, 2(2012)1, pp. 12-16.
- [40] Ali, S.A., Vathsal, S. & Kishore, K.L. An efficient denoising technique for CT images using window-based multi-wavelet transformation and thresholding. *European Journal of Scientific Research*, 48(2010)2, pp. 315-325.
- [41] Yussof, W.N.J.W. & Burkhardt, H. 3D volumetric CT liver segmentation using hybrid segmentation techniques. *Proceedings of the International Conference of Soft Computing and Pattern Recognition*, Malacca, Malaysia, 4-7 Decemeber, 2009, IEEE, pp. 404-408.
- [42] Krátký, J. & Kybic, J. Three-dimensional segmentation of bones from CT and MRI using fast level sets. *Proceedings of the SPIE Medical Imaging Conference*, San Diego, California, United States, 16-21 February, 2008, SPIE, Vol. 6914, 10 pp.
- [43] Veldkamp, W.J., Joemai, R.M., van der Molen, A.J. & Geleijns, J. Development and validation of segmentation and interpolation techniques in sinograms for metal artifact suppression in CT. *Medical Physics*, 37(2011)2, pp. 620-628.
- [44] Molteni, R. From CT numbers to Hounsfield Units in cone beam volumetric Imaging: the effect off artifacts. Chicago 2011. AAOMR. Unpublished presentation. 47 p.
- [45] Feldkamp, L.A., Davis, L.C. & Kress, J.W. Practical cone-beam algorithm. *Journal of the Optical Society of America A*, 1(1984)6, pp. 612-619.
- [46] Bornard, R., Lecan, E., Laborelli, L. & Chenot, J.-H. Missing data correction in still images and image sequences. *Proceedings of the Tenth ACM International Conference on Multimedia*, Juan-les-Pins, France, 1-6 December, 2002, ACM, pp. 355-361.
- [47] Ignácio, U.A. & Jung, C.R. Block-based image inpainting in the wavelet domain. *The Visual Computer: International Journal of Computer Graphics*, 23(2007)9, pp. 733-741.
- [48] Brito-Loeza, K. & Chen, K. Multigrid method for a modified curvature driven diffusion model for image inpainting. *Journal of Computational Mathematics*, 26(2008)6, pp. 856-875.
- [49] Li, Y., Chen, Y., Hu, Y., Oukili, A., Luo, L., Chen, W. & Toumoulin, C. Strategy of computed tomography sinogram inpainting based on sinusoid-like curve decomposition and eigenvector-guided interpolation. *Journal of the Optical Society of America A*, 29(2012)1, pp. 153-163.
- [50] Bornemann, F. & März, T. Fast image inpainting based on coherence transport. *Journal of Mathematical Imaging and Vision*, 28(2007)3, pp 259-278.

- [51] Naylor, P.J. Profiling, Optimization, and Acceleration of MATLAB code. [WWW]. [Accessed on 13.04.2013]. Available at: http://www.sal.ufl.edu/NewComers/matlab_optimization.pdf
- [52] MATLAB. Parallel-computing toolbox. [WWW]. [Accessed on 13.04.2013]. Available at: <http://www.mathworks.se/products/parallel-computing/>
- [53] Gong, M., Langille, A. & Gong, M. Real-Time Image Processing Using Graphics Hardware: A Performance Study. Proceeding of the Second International Conference on Image Analysis and Recognition, Toronto, Canada, 28-30 September, 2005, Springer Verlag, vol. 3656, pp. 1217-1225.